

ABSTRACT

WATER DROPLET BEHAVIOR ON AN ANISOTROPIC ALUMINUM FIN— A CASE STUDY IN SURFACE WETTABILITY MODIFICATION AND CONTROL

by Jia Ying

A new method is reported for creating patterned aluminum surfaces using standard photolithographic practices to create micro-scale channels on the surface. Water droplet behavior on these surfaces is measured to study the effect of the anisotropic, micro-scale channels on the overall surface wettability and critical droplet size. Experimental data show that these functionalized surfaces exhibit decreased contact angle hysteresis, and a reduction in the volume needed for the onset of droplet sliding is observed. Additionally, for injected droplets, the required air-flow rate for the onset of water droplet drainage is decreased. Motivated by these findings, a model is developed to predict the critical air-flow rate for droplet movement on the fin surface, and a new method for fabricating hydrophobic stripes on the surface has also been explored. These results which show the promise of these functionalized surfaces for improved condensate management may be used to guide future fin surface design in heat exchangers.

WATER DROPLET BEHAVIOR ON AN ANISOTROPIC
ALUMINUMFIN— A CASE STUDY IN SURFACE WETTABILITY
MODIFICATION AND CONTROL

A Thesis

Submitted to the

Faculty of Miami University

in partial fulfillment of

the requirement for the degree of

Master of Science

Department of Physics

by

Jia Ying

Miami University

Oxford, Ohio

2010

Advisor_____

ANDREW D. SOMMERS/ KHALID F. EID

Reader_____

LEI L. KERR

Reader_____

PAUL K. URAYAMA

Table of Contents

<i>Table of Contents</i>	<i>ii</i>
<i>List of Tables</i>	<i>iv</i>
<i>List of Figures</i>	<i>iv</i>
<i>Nomenclature</i>	<i>viii</i>
<i>Acknowledgements</i>	<i>x</i>
 <i>Chapter 1. Introduction</i>	 <i>1</i>
1.1 Background	1
1.2 Literature Review	2
1.2.1 Surface Fabrication	2
1.2.2 Modeling Condensate Retention.....	4
<i>Chapter 2. Experimental Methods and Apparatus</i>	<i>7</i>
2.1 Materials and Sample Preparation.....	7
2.1.1 Surface Preparation.....	7
2.1.2 Photolithographic Method	7
2.1.3 Surface Modification	9
2.2 Contact Angle Measurement	11
2.3 Critical Inclination Angle Measurement	12
2.4 Airflow Induced Droplet Movement	13
2.5 Condensed Droplet Experiments.....	15
2.6 Water Droplet Evaporation Rate	16
<i>Chapter 3 Results and Discussion</i>	<i>19</i>
3.1 Contact Angle Data.....	19
3.1.1 Wenzel's Model.....	19
3.1.2 Advancing and Receding Contact Angle	19
3.2 Critical Inclination Angle Data	21
3.2.1 Data Analyses and Model Prediction	21
3.2.2 Critical Inclination Data for Condensed Droplets	24
3.3 Wind Tunnel Test Data	26
<i>Chapter 4 Water Droplet Modeling</i>	<i>29</i>

4.1 Related Modeling Work.....	29
4.1.1 An Existing Model.....	29
4.1.2 Surface Tension Force Calculation.....	30
4.2 Development of a New Model	32
4.2.1 Air Flow Force	32
4.2.2 Droplet Projected Area.....	32
4.2.3 Droplet Diameter vs. Droplet Volume.....	34
4.2.4 Drag Coefficient.....	35
4.2.5 Surface Tension Force	38
4.2.6 Angle of Movement on a Vertical Surface.....	39
4.2.7 Surface Tension Force on Anisotropic Surfaces:	42
4.3 Results and Conclusion.....	43
4.3.1 Model Predictions on a Vertical Baseline Surface	44
4.3.2 Droplet Behavior on a Vertical Anisotropic Surface.....	45
<i>Chapter 5 Manufacturing Surfaces with Chemical Stripes</i>	<i>49</i>
5.1 Literature Review	49
5.2 Experimental Methods.....	49
5.2.1 Electro deposition Process	50
5.2.2 Thermal Stability Test.....	52
5.2.3 Creating Micro-channel Stripes with Super-hydrophobic Material	53
5.3 Results and Conclusion.....	55
<i>Chapter 6 Conclusion and Recommendations.....</i>	<i>58</i>
6.1 Summary of Results.....	58
6.1.1 Surface Manufacturing.....	58
6.1.2 Surface Parameter Measurements	58
6.1.3 Water Droplet Modeling	60
6.1.4 Manufacturing of hydrophobic stripes.....	61
6.2 Recommendations for Future Work.....	62
<i>References</i>	<i>64</i>
<i>Appendix A: Model for Horizontal Surfaces.....</i>	<i>67</i>
<i>Appendix B: Model for Vertical Surfaces</i>	<i>69</i>

List of Tables

Table 1: Standard photolithographic process performed on Al plates	10
Table 2: Matrix of Test Samples	20
Table 3: Contact angle for baseline surface	21
Table 4: Contact angle data for Sample 1 (with no coating and micro-channels 10 μ m deep)	21
Table 5: Contact angle data for Sample 1 (with PDMS and micro-channels 10 μ m deep)....	21
Table 6: Contact angle data for Sample 2 (with PDMS and micro-channels 6.8 μ m deep) ..	21
Table 7 Droplet Volume, “Blow-Off” Velocity, Reynolds Number for the Baseline and C_d	37
Table 8: Angle of Movement on a Vertical Baseline Surface	41

List of Figures

Figure 1.1 Force balance on a drop on an inclined surface. F_g , F_s , and F_d are the forces due to gravity, surface tension, and drag, respectively [16].	6
Figure 2.1 Microscope images of an Al surface: (a) Al surface cleaned with acetone and DI water; (b) Al surface immersed in 4 wt% NaOH for two hours	8
Figure 2.2 Myriad System 2001 Mask Aligner	10
Figure 2.3 Photomask containing five distinct regions	10
Figure 2.4: SEM images of Al surfaces after etching with Transene Aluminum Etchant Type A for 30 minute: (a) 15 μm wide parallel channels, (b) 50 μm wide parallel channels.	10
Figure 2.5: Chemical structure of poly(dimethylsiloxane) vinyl terminated (PDMSVT)	11
Figure 2.6 RaméHart precision contact angle goniometer	12
Figure 2.7 Apparent contact angle for water on Al surface	12
Figure 2.8 Tilt-table for measuring the critical inclination angles	13
Figure 2.9 A droplet sliding on a tilted surface	13
Figure 2.10 Schematic of the AEROLAB Educational Wind Tunnel System	14
Figure 2.11 Wind tunnel test section	15
Figure 2.12 Environmentally-Controlled Condensation Chamber	16
Figure 2.13 Weight of water drops (on Al surface) as a function of time. Drop weights are 0.0106g (shown in blue) and 0.000549g (black)	18
Figure 3.1 Wenzel's model	19
Figure 3.2: Critical inclination angle data for droplets on baseline surface, sample 1 and sample 2	23
Figure 3.3 (a) Droplet moves parallel to the direction of channels; (b) Droplet moves perpendicular to the direction of channels	22

Figure 3.4: Critical inclination angle data on sample 1 for droplets moving \perp to the channels and $//$ to the channels	23
Figure 3.5: Experimental data for the (a) baseline surface, (b) sample 1, and (c) sample 2 compared with the predicted critical inclination angle using the Dussan equation [27]	24
Figure 3.6 20 μ L condensate droplet (left) and injected droplet (right) on Sample 1	25
Figure 3.7: Critical inclination data for condensate droplets on the baseline surface and sample 1	25
Figure 3.8 Baseline surface: inclination angle for condensate(red) and injected (black) droplets.....	26
Figure 3.9 Sample 1: inclination angle for condensate(blue) and injected(black) droplets..	26
Figure 3.10: Critical air-flow rates required for droplet motion on: (a) the baseline surface and sample 3, and (b) the baseline surface and sample 1 in both the parallel and perpendicular configurations.....	28
Figure 4.1: Force balance on a drop on an inclined plane with elliptical contour [28]	30
Figure 4.2 Parallel-sided droplet	31
Figure 4.3 Force balance on a vertical surface with air flow	32
Figure 4.4: Schematic of the “two-circle” method [26]	33
Figure 4.5 Profile of droplets fits a circle.	35
Figure 4.6 Side image of a droplet on a vertical baseline surface	35
Figure 4.7 Droplet volume (m^3)(x-axis) vs. droplet diameter (m)(y-axis):data points shown in blue assumed a circular contact line; experimental data on a vertical surface are shown in red	35
Figure 4.8 A horizontal surface in wind tunnel.....	37
Figure 4.9 Equipment used for angle measurement: wind tunnel, CCD camera, tripod, light source and a laptop	40
Figure 4.10: Track of a droplet on vertical surface with air-flow from right to left	40

Figure 4.11 (a) Droplet image at $t=0$ (b) Droplet images after sliding	41
Figure 4.12 A substrate of high surface energy satisfying Wenzel's mode of wetting	43
Figure 4.13 Model prediction of the critical air-flow velocity (blue curve) and experimental data (red)	44
Figure 4.14 Model prediction for baseline (blue curve) Sample 1 (black curve) and their experimental data.....	47
Figure 4.15 Model prediction for sample 2 (green curve) and experimental data of sample 2 and sample 1	47
Figure 4.16 Model prediction for sample 3 (blue curve) and experimental data (green curve)	48
Figure 4.17 Model prediction for sample 3 (blue curve) and and baseline surface (green curve).....	48
Figure 5.1 Electro-deposition processes.....	51
Figure 5.2 A droplet on the copper surface: apparent contact angle 131.9 degree	52
Figure 5.3 SEM images of flower-like clusters on copper surface.....	52
Figure 5.4 Surface with contact angle of 108 degree after baked at 100°C for 10 min.....	53
Figure 5.5 SEM image of surface after baked at 100°C for 10 min	53
Figure 5.6 Microscope image of the copper surface with stripes (black).....	55
Figure 5.7 SEM images of copper surface with stripes.....	56
Figure 5.8 Surface with stripes: contact angle on the left is larger than right.....	56
Figure 5.9 Top image of a small droplet on the surface with stripes.	57

Nomenclature

A_{pr}	projected area
A	scaling factor of surface tension force
C_d	drag coefficient
D	diameter of droplet
F_d	drag force
F_g	gravitational force
F_{gx}	gravitational force in the x-direction
F_s	surface-tension force
F_{sx}	surface-tension force in the x-direction
g	acceleration of gravity
k	surface-tension force factor
$L1, L2$	distances defined in Figure 4.4
Lf	ratio defined in Eq. 4.15
m	mass of drops
R	drop radius
Re	Reynolds number
u	air velocity
V	volume
w	drop width
x, y, z	coordinates

Greek Symbols

α	critical inclination angle of a surface from the horizontal
β_1	angle defined in eq.4.18
φ	angle of movement on a vertical surface
ϕ	azimuthal angle
θ	contact angle
θ_A	advancing contact angle

θ_R	receding contact angle
γ	liquid surface tension
ρ_a	density of air
μ	viscosity
ψ	ratio defined in Eq.4.30

Acknowledgements

It is a pleasure to thank those who made this thesis possible.

It is difficult to overstate my gratitude to my advisors, Dr. Andrew D. Sommers and Dr. Khalid F. Eid. With their enthusiasm, inspiration, and their great efforts to explain things clearly and simply, they helped to make this project fun for me. Throughout my two years study in Miami University, they provided encouragements, sound advices, good teaching, good company and lots of good ideas. I would have been lost without them.

I am also grateful and would like to acknowledge financial support from the American Society of Heating, Refrigerating, and Air-Conditioning Engineers (ASHRAE) and Sapa Heat Transfer.

Last but not least, I would like to thank my parents, Mr. and Mrs. Ying, for their absolute confidence in me. The knowledge that they will always be there to pick up the pieces is what allows me to take risks in my life and study. To them I dedicate this thesis.

Chapter 1. Introduction

1.1 Background

Heat exchangers are important to the overall efficiency, cost, and compactness of heating, ventilation, air-conditioning and refrigeration (HVAC&R) systems. According to a 2007 Department of Energy study, the heating, cooling, and lighting of residential and commercial buildings accounts for almost 16% of the United States' total energy consumption[1], and Ohio ranks sixth among states in its overall energy consumption—having consumed more than 4,000 trillion BTUs of total energy in 2004[2].

Current fin-and-tube and plate heat exchanger designs rely heavily on copper and aluminum which are naturally hydrophilic. When moist air comes in contact with a heat exchanger operating below the dew point, condensate occurs on the heat transfer surface. Once condensate forms, it will continue to accumulate on the surface until it is removed by either gravitational or air-flow forces. In a broad range of air-cooling applications, water retention on the heat transfer surface is problematic because it can decrease the overall energy efficiency of the heat exchanger by reducing the sensible heat transfer coefficient, increasing the air-side pressure drop, and providing a site for biological activity. In refrigeration systems, the accumulation of frost on the heat exchanger requires periodic defrosting which carries an accompanying energy expenditure. Thus the drainage of water either due to condensation or melting frost is very important to the overall performance of heat transfer systems.

Although chemical modification is a common method for manipulating surface wettability, the usual approach in the literature is to uniformly modify the surface by chemical treatment. In HVAC&R applications, controlling the direction of condensate movement on the surface is as important as the physical removal of those droplets. Homogeneously modified surfaces would permit condensate blow-off into the occupied space which is undesirable. Therefore, a surface with an anisotropic, patterned wettability is preferred since droplet motion can be restricted to one direction—downward with gravity. **The objective of this research was to investigate**

alternative ways of inexpensively manufacturing such surfaces and to evaluate the behavior and retention of water droplets on an aluminum surface that had been functionalized using micro-channels and poly(dimethylsiloxane) (PDMS) to alter the surface wettability. Because the retention of water on the heat transfer surface in air-cooling applications can affect the thermal-hydraulic performance, new competing technologies are needed for the design of future high performance, energy-efficient heat exchangers.

This work also sought to develop a model that could be used to predict the critical air-side flow rate necessary for droplet shedding on a heat transfer surface as a function of the contact angles, micro-channel surface geometry and water droplet volume. Experiments were performed to gather data for validating the model. The so-called critical droplet is a droplet large enough that the surface tension retaining force is equal to the combined gravitational and air-flow (if applicable) drainage force—that is, the critical droplet refers to a droplet at the condition of incipient motion. Therefore, understanding the behavior, shape, and size of the critical droplet is the key to understanding droplet retention on the heat transfer surface. The developed model could then be used by designers to assess possible trade-offs in future fin surface designs and to avoid potential condensate “blow-off” conditions. The model could also be used with water droplet size distribution functions to predict the quantity of retained condensate on the heat exchanger.

1.2 Literature Review

1.2.1 Surface Fabrication

Although extensive research has been reported on using topography and chemistry to alter surface wettability in other applications, few studies exist on the use of these techniques in conventional HVAC&R systems where the energy impact could potentially be quite large. In fact, very few papers have been published on the hydrophobizing of metal substrates, and studies concerned with the manufacture of hydrophobic aluminum surfaces are especially rare in the literature. H. Tavana and coworkers [3] fabricated superhydrophobic surfaces of *n*-hexatriacontane in a

single-step process with silicon wafers selected as the substrate. The average advancing and receding contact angles were reported as 170.9° and 165.0° , respectively. Zhang, *et al* have reported an easy method of patterning hydrophilic-hydrophobic stripes over TiO_2 surfaces by the selective photocatalytic decomposition of octadecylphosphonic acid (ODP) monolayers via UV irradiation[4]. However, information about patterning other metal surfaces is not provided. L. Rizzello, *et al* [5] focus on fabricate nanorough metallic substrates with efficient hydrophobic or hydrophilic properties using spontaneous galvanic displacement reactions (SGDR) to roughen flat silver (Ag) or silicon (Si) substrates to create nanostructured gold films. The deposition of long polar molecules, such as octadecylamine (ODA), onto the optimized nanorough surface resulted in hydrophobic behavior with the water contact angle increased to 135° . However, increasing further the surface hydrophobicity using this procedure resulted in the fabrication of nonuniform substrates with nonreproducible water contact angle values. Shibuichi, *et al.* and Qian and Shen describe wet chemistry techniques for producing hydrophobic aluminum surfaces [6, 7]. These methods produce many cracks and small rectangular pits in the surface which could be problematic in applications where thermal cycling is necessary. Subsequently, these methods also require treatment of the surface via fluoroalkylsilanes and do not lend themselves to detailed surface patterning. Guo, *et al.* obtained super-hydrophobic aluminum alloy 2024 surfaces using wet chemical etching followed by modification of the surface with a cross-linked silicone elastomer, perfluorononane (C_9F_{20}), or perfluoropolyether (PFPE) [8]. Water contact angles exceeding 150° were achieved, and Guo, *et al.* concluded that the effects of surface roughness resulted from the etching time, and the concentration of NaOH aqueous solution plays a very important role in the fabrication of a super-hydrophobic surface. Bayiati, *et al.* focused on the selective deposition of fluorocarbon (FC) films on metal surfaces, specifically aluminum, in an effort to control surface wettability [9]. In this study, C_4F_8 , CHF_3 , and CHF_3/CH_4 fluorocarbon gases were selected and plasma parameters were varied to achieve optimal deposition selectivity. Hydrophobic surface properties were achieved. The maximum achievable water contact angle using this

method was 118°, and water droplets deposited on the modified Al surfaces for long times were observed to penetrate the film. Ji, *et al.* deposited hydrophobic multilayer CF_x coatings on aluminum using benign Ar/C₂H₂/C₃F₈ chemistry in a sputtering/plasma-enhanced chemical vapor deposition system [10]. The degree of hydrophobicity was observed to depend both on the fluorine content of the coating and the surface morphology. Because of problems with adhesion on aluminum, a chromium intermediate layer had to be deposited onto the Al substrate first before the CF_x coating could be deposited. Somlo and Gupta prepared a weakly hydrophobic 6061 aluminum alloy surface through a dipping process involving dimethyl-*n*-octadecylchlorosilane (DMOCS) and studied the tensile strength of the ice/DMOCS interface [11]. No contact angle information was provided, and the adherence and longevity of the DMOCS coating to the aluminum surface was not quantified. Sommers and Jacobi demonstrated that functionalized aluminum surfaces with an anisotropic, micro-scale topography can be used to both manipulate the critical droplet size and affect the overall surface wettability [12]. Such surfaces have also been shown to retain less water than conventional aluminum heat transfer surfaces. However, these improvements necessitated the use of a novel, anisotropic dry-etching technique to chemically erode the surface using a chlorine-based plasma. The cost associated with fabricating these surfaces is currently quite high. Therefore, the future success and implementation of this design will likely require new, innovative methods of manufacturing anisotropic fins.

1.2.2 Modeling Condensate Retention

A simple model for predicting the amount of condensate retained on plain-fin heat exchangers was developed by Korte and Jacobi [13, 14]. The volume of retained condensate was obtained by integrating the number of drops of a given size, D , multiplied by the volume of a drop of that size, for all drops.

$$m_D = \rho \iint n_D(D) V(D) dD dA \quad (1.1)$$

where ρ is the liquid density, $n_D(D)$ is the number of drops of a given size D per unit

area, and $V(D)$ is the volume of a drop of size D . The double integration is performed for all drop sizes. The size distribution function, $n_D(D)$, was fitted by a logarithmic function, based on the data of Graham [18],

$$\begin{aligned} n_{Ds} &= 5.104 (10^6) D^{-2.37} & \text{for } 10\mu\text{m} \leq D \leq 0.2D_{\text{max}} & \quad (1.2a) \\ \text{and} \quad n_{Db} &= 1.117 (10^{10}) D^{-3.8} & \text{for } 0.2D_{\text{max}} \leq D \leq D_{\text{max}} & \quad (1.2b) \end{aligned}$$

where n_{Ds} and n_{Db} denote distributions for small and big drops, respectively. The maximum drop diameter, D_{max} , was needed to set the integration limits and determine the size-distribution function, n_D . The maximum diameter was determined from a balance of gravitational, surface tension, and air-flow forces on a drop, as shown in Figure 1.1. The model of Korte and Jacobi [16] showed reasonable success in predicting the amount of condensate retained on one heat exchanger. However, simplifications were made related to droplet shapes which affected the predictions of the volume function, $V(D)$, and the maximum diameter. All drops were assumed to be spherical-caps with maximum and minimum angles equal to the advancing and receding angles of the surface. In calculating surface tension forces, the contact angles were assumed to vary linearly with the azimuthal angle. Thus, the model was a bit limited in its overall accuracy and applicability.

Most investigations of drops on inclined surfaces focus on the special case of water drops at sliding condition. Important parameters such as maximum diameter, maximum volume, and critical contact angles can all be obtained by studying this special case. Merte and Yamali [19] studied two-dimensional droplets on vertical surfaces at the critical condition of sliding. The advancing contact angle and drop diameter were specified as inputs, while the receding angle and profile were calculated as outputs. The total energy for droplets of a given volume was then minimized using variational calculus. However, they did not measure the advancing contact angle for the tested surface. Instead, they used a value for θ_A that best fit their data. This two-dimensional analysis neglected the variation of contact angles along the droplet which can affect surface-tension forces. Also, they assumed a circular contact line in order to determine the droplet diameter.

In a related work, Goodwin *et al* [20] presented a simplified model for drop

detachment from a rotating disk and measured critical rotational speeds. They also measured the maximum droplet volume and contact angles for various liquids on vertical surfaces.

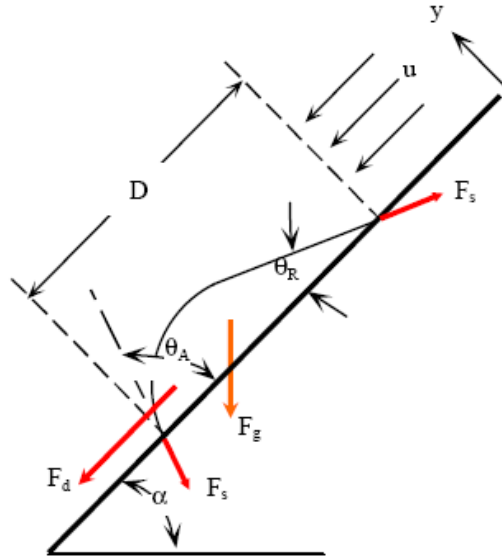


Figure 1.1 Force balance on a drop on an inclined surface. F_g , F_s , and F_d are the forces due to gravity, surface tension, and drag, respectively [16].

Chapter 2. Experimental Methods and Apparatus

The methods of surface fabrication, contact angle measurements, critical inclination measurements and wind tunnel tests are presented in this chapter. The experimental apparatus and instrumentation are also described.

The experimental apparatus consisted of a Myriad mask aligner, a Ramé-Hart contact angle goniometer, a custom-built tilt-table assembly, and a subsonic wind tunnel. Other equipment used during the course of this research includes a photoresist spinner, CCD cameras, a Sartorius electronic balance, and a Gilmont micro-syringe for injecting droplets.

2.1 Materials and Sample Preparation

2.1.1 Surface Preparation

This research builds upon a technique developed by Guo, *et al.* who increased the water contact angle from about 67° to more than 160° by immersing an aluminum surface in sodium hydroxide for several hours and then spin coating a layer of poly(dimethylsiloxane) vinyl terminated (PDMSVT) on the surface [11]. This observed change in the water droplet contact angle was explained using Cassie's model of wetting [21].

In this research, aluminum plates (2.5 by 2.5 inches in size) were constructed from Al alloy 1100. The plates were first cleaned with acetone for 15 minutes in an ultrasonic bath and then dried using a stream of nitrogen gas (shown in Fig. 2.1a). Next, the plates were pre-roughened by immersing in 4 wt% NaOH aqueous solution for 2 hours to increase the initial surface roughness. Following this process, uniformly distributed surface protrusions, were observed on the substrate (see Fig. 2.1b).

2.1.2 Photolithographic Method

Standard photolithographic practices were then used to prepare the plates for wet etching and chemical treatment. Photolithography uses light to transfer a geometric pattern from a photo mask to a light sensitive photo resist on the surface. A series of

chemical treatments can then be performed to etch the exposure pattern into the underlying material. Prior to this process, the plates were chemically cleaned to remove contamination and heated to drive off any moisture that may be present on the surface.

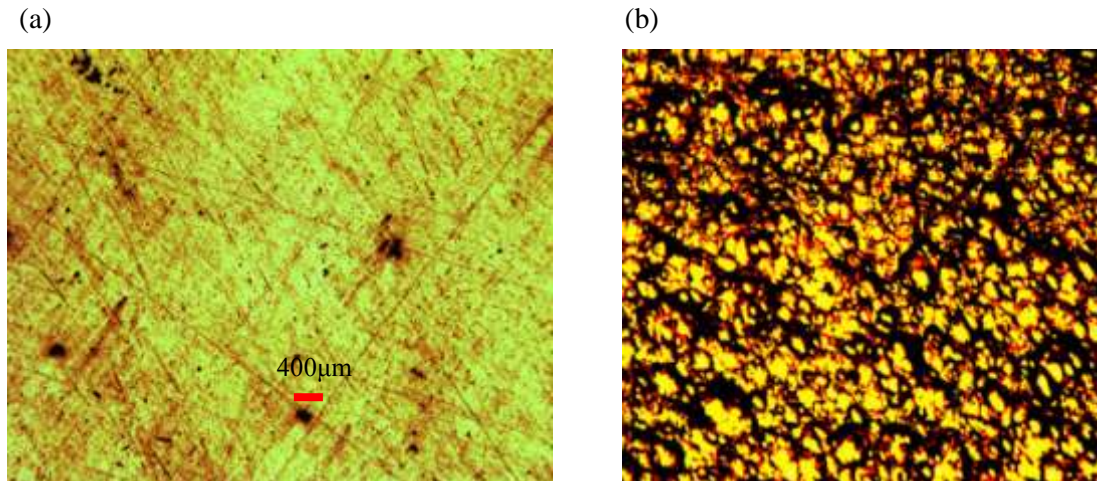


Figure 2.1 Microscope images of an Al surface: (a) Al surface cleaned with acetone and DI water; (b) Al surface immersed in 4 wt% NaOH for two hours

First, a positive photoresist (i.e. S1813) was spin-coated onto the aluminum surface. A liquid solution of photoresist was dispensed onto the plate, and the plate was spun rapidly using a high speed spinner (Laurell Spinner Model WS400B-6NPP/LITE) to produce a uniformly thick layer. The thickness of S1813 layer was $1.8\mu\text{m}$ when spun at 2000 rpm for 40 seconds. Because the total energy needed for proper exposure is dependent on the thickness of the film, a thin and homogeneous film is necessary for high resolution.

Following this process, the aluminum plate was soft baked to prevent mask sticking, and a Myriad System 2001 Mask Aligner (see Figure 2.2) was used to align the photomask over the aluminum substrate and expose the photoresist to UV light. The photomask used in this project contained different size parallel micro-grooves ($15\mu\text{m}$, $50\mu\text{m}$, $100\mu\text{m}$) as shown in Fig. 2.3. A special region with “dashed” $15\mu\text{m}$ wide channels was created on the mask. The spaces between channels increase from $5\mu\text{m}$ to $50\mu\text{m}$. It is important to ensure that the correct exposure time is used during this process. For a positive photoresist, if underexposed, there will be areas of resist

remaining after development. If overexposed, the reflection of light off the substrate and the refraction of light through the mask can cause the protected area to become exposed. After exposure, the plate was developed using the Shipley Microposit Developer CD-26. The S1813 photoresist is soluble in the CD-26 developer following UV exposure, whereas for a negative photoresist (such as KMPR 10015), the exposed regions are insoluble. Table 1 shows the relevant photolithography parameters.

Following the photolithographic process, the surfaces were etched using Transene Aluminum Etchant Type A (an acid solution consisting of 80 wt% phosphoric acid, 5% nitric acid, 5% acetic acid, and 10% distilled water) at 50°C with an etching rate of approximately 660 nm/min.

2.1.3 Surface Modification

After etching, the photoresist was then stripped in acetone and the plates were rinsed in DI water for 3 minutes and characterized using a surface profilometer. The measured depth of the channels after etching for 25 and 30 minutes were 6.8 μ m and 10 μ m, respectively. The microchannels were then imaged on a Field Emission Scanning Electron Microscope (FE-SEM) as shown Fig. 2.4.

Further surface modification was performed using poly(dimethylsiloxane) vinyl terminated (PDMSVT) purchased from Sigma–Aldrich, USA (shown in Fig. 2.5) in combination with 1 wt% 184 curing agent obtained from Dow Corning Company. The modified films were obtained by spin-coating at a speed of 3000 rpm for 30 seconds and then curing on a hot plate for 20 minutes. By spinning at 3000 rpm, the PDMSVT formed a relatively thick film on the surface (approx. 13 μ m). PDMSVT is a low surface energy material which can be used to increase the hydrophobicity of the underlying surface. This hydrophobicity is further amplified by the roughness of the underlying substrate.



Figure 2.2 Myriad System 2001 Mask Aligner

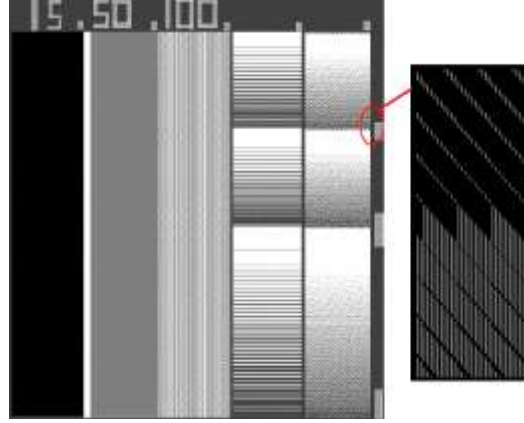


Figure 2.3 Photomask containing five distinct regions: (1) 15 μm wide parallel stripes, (2) 50 μm wide parallel stripes, (3) 100 μm wide parallel stripes, (4) vertical wettability gradient(15 μm wide parallel stripes) , and (5) wettability gradient at a 45°

Table 1: Standard photolithographic process performed on Al plates

Photoresist	Spinning	Soft Bake	Exposure	Developer	Post Bake
S1813	40 sec @ 2000 rpm	110 °C 1 min	3 sec	CD-16 (40s)	125 °C 2 min

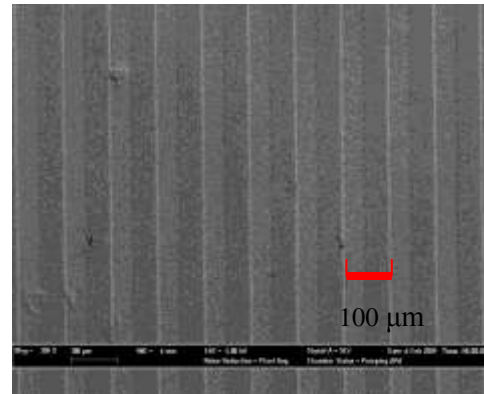
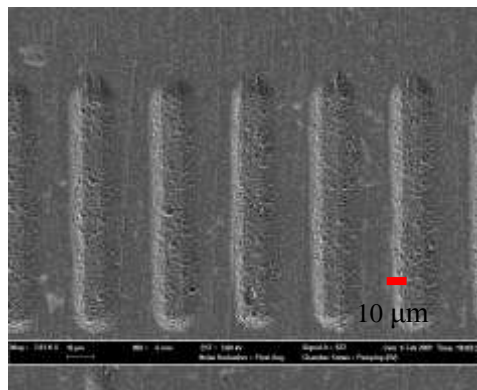


Figure 2.4: SEM images of Al surfaces after etching with Transene Aluminum Etchant Type A for 30 minute: (a) 15 μm wide parallel channels, (b) 50 μm wide parallel channels.

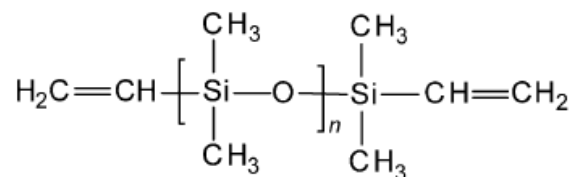


Figure 2.5: Chemical structure of poly(dimethylsiloxane) vinyl terminated (PDMSVT)

2.2 Contact Angle Measurement

Information about the advancing and receding contact angles of water droplets injected onto these fabricated surfaces was obtained using a RaméHart precision contact angle goniometer (see Fig. 2.6) and compared among the surfaces.

Contact angle can be measured by producing a water droplet on the test surface. The angle formed between the Al/water interface and the water/air interface (which has a vertex where the three interfaces meet) is referred to as the contact angle (see Fig. 2.7). Contact angle is a primary tool used to measure surface cleanliness and is also frequently used to characterize the wettability of the surface. A droplet with a large contact angle (i.e. $\theta > 90^\circ$) occurs where the solid surface free energy is low and is referred to as “hydrophobic.” A droplet with a small contact angle occurs on a surface that is “hydrophilic.”

The advancing contact angle is measured by adding water to the droplet dynamically without increasing the interfacial area between the liquid and solid phases until the maximum volume is achieved. The resulting contact angle is referred to as the advancing angle. To measure the receding contact angle, water is then removed from the droplet. When the minimum volume that can be removed without reducing the solid/liquid interface is reached, the resulting contact angle is measured. This angle is referred to as the receding angle. The advancing and receding angles were measured at different locations on each sample to ensure greater accuracy. The average measurements are reported in Chapter 3. The maximum uncertainty in these measured contact angles was less than 1° .

When the receding angle is subtracted from the advancing angle, the difference is called the *contact angle hysteresis*. The hysteresis which characterizes the surface

wettability is used to quantify contamination, surface chemical heterogeneity, and the effect of surface treatments. Surfaces with lower contact hysteresis generally retain less water than those with high contact angle hysteresis.

2.3 Critical Inclination Angle Measurement

The critical inclination angle for sliding on different surfaces was measured using a tilt-table assembly with an extendable lever arm that permitted continuous inclination of the surface from horizontal (see Fig. 2.8). After a droplet was injected on the test sample in the horizontal position using a micro-syringe, the plate was then slowly tilted until imminent droplet motion was detected (see Fig. 2.9). A KAPPA DX 10-1394a high-resolution CCD camera was used to record profile images of the droplets from a location parallel to the base. Prior to droplet injection, test images were recorded for calibration purposes. Multiple measurements were recorded for each droplet volume which permitted the critical inclination angle and related droplet diameter to be checked for consistency. The uncertainty in the measured critical inclination angle ranged from $\pm 2^\circ$ - 10° with the largest uncertainty occurring at small droplet volumes. The typical uncertainty of these measurements was $\pm 2^\circ$ - 3° .



Figure 2.6 Ramé-Hart precision contact angle goniometer

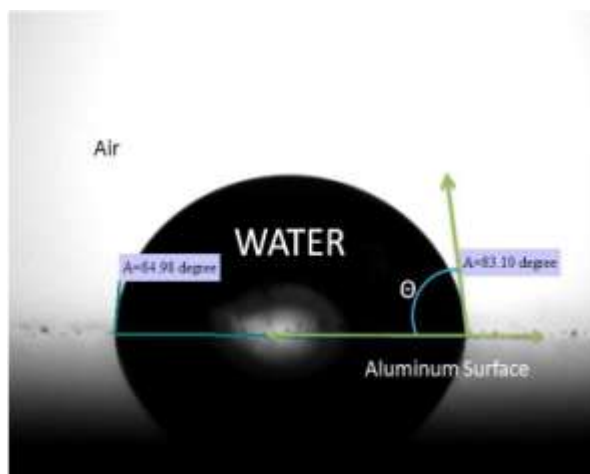


Figure 2.7 Apparent contact angle for water on an Al surface

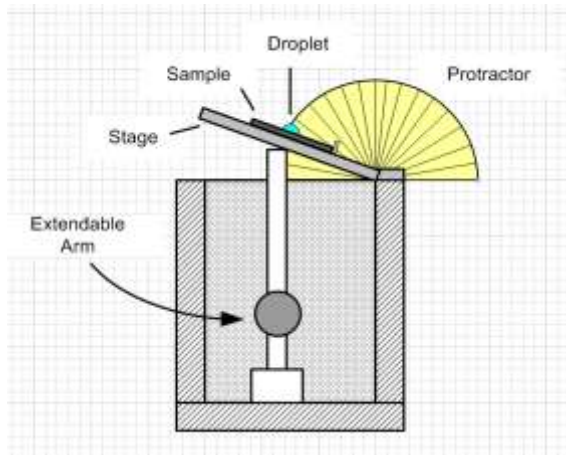


Figure. 2.8 Tilt-table for measuring the critical inclination angle

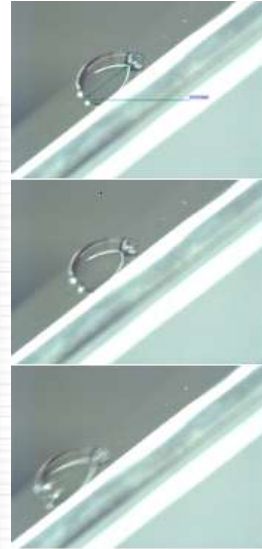


Figure 2.9 A droplet sliding on a tilted surface

2.4 Airflow Induced Droplet Movement

An AEROLAB subsonic wind tunnel was used to study the critical velocity for airflow induced droplet movement as illustrated in Figure 2.10. This open circuit wind tunnel does not directly re-circulate air. Instead, the air is drawn in from the laboratory environment through an aluminum honeycomb flow straightener which is used to condition the incoming air. The contraction section is bell-shaped, and the contraction ratio is 9.5:1. The test section ($12'' \times 12'' \times 24$) of this wind tunnel is constructed using anodized 6061 aluminum with two top-hinged acrylic side windows and one top window to allow optical access. To compensate for boundary layer growth within the test section, the side walls diverge slightly. The specified airspeed range for this wind tunnel is 4.5 m/s to 65+ m/s with an associated turbulence level of less than 0.2%.

In HVAC&R applications with simultaneous heat and mass transfer, air flow across a fin surface containing condensed water is common. As shown in Figure 2.11, experiments were conducted in the wind tunnel test section to measure the air-flow force required to overcome the surface tension retaining force and cause water droplet motion (i.e. the incipience of “droplet blow-off”).

For these experiments, the aluminum test sample was fixed inside the wind

tunnel parallel to the direction of the air stream. After a water droplet of known volume was injected onto the sample by micro-syringe, then the blower was activated. If droplet motion was not immediately observed, the fan was turned “off.” The fan speed was then incrementally increased using a PID controller, and a new droplet was placed on the sample. When droplet motion was first detected, the air velocity was measured using a hot-bulb anemometer to determine the “critical airflow rate” for droplet motion for a given size on the test surface. The anemometer was placed 2.43 inches away from the test sample. For the flow rates examined in these experiments, the local velocity at the droplet half height was taken as equal to the measured mainstream velocity since the boundary layer is thin. (According to the Blasius velocity profile, the local velocity at the droplet half height is within 99.9% of the mainstream velocity for the location on the surface where the droplet was placed.) Because a new droplet was placed on the surface prior to each performed test and uniform flow conditions are achieved soon after the activation of the fan, losses due to evaporation were assumed to be minimal.

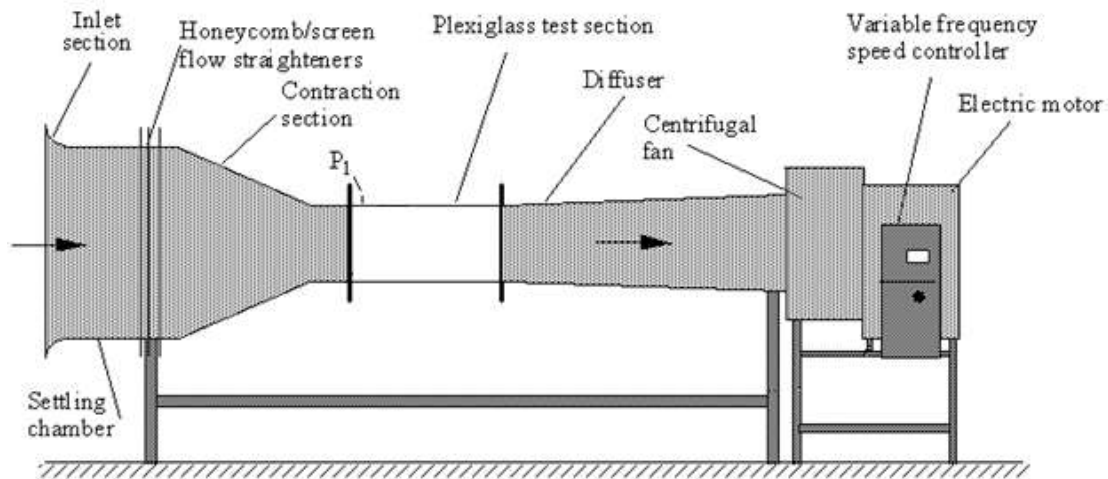


Figure 2.10 Schematic of the AEROLAB Educational Wind Tunnel System

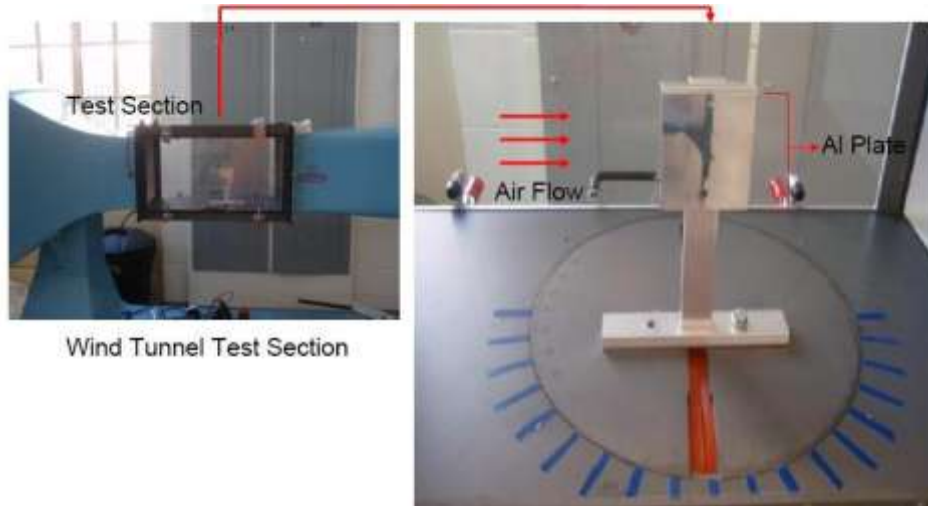


Figure 2.11 Wind tunnel test section

2.5 Condensed Droplet Experiments

For the measurement of water droplet contact angles and critical sliding angles, the water droplet can originate on the surface in one of two ways: by injection onto the surface using a micro-syringe or by condensing water vapor onto the surface using a condensation chamber (see Figure 2.12). In these experiments, water was condensed onto the test sample using a Peltier cooler inside an environmentally-controlled chamber. An ultrasonic cool mist humidifier was used to maintain the relative humidity to within 3% inside the enclosure, and a thermoelectric cooler was used to lower the temperature of the substrate. A DC power supply (20V) was used to support the thermoelectric cooler. A thermometer was connected to test sample directly to measure the surface temperature, and a humidity meter was used to measure the environmental humidity inside the enclosure.

In these experiments, the thermoelectric cooler was started first to pre-cool the surface to a lower temperature. Then, the humidifier was turned on to maintain the humidity of 70%. Both the cooler and humidifier were turned on/off periodically to control the humidity and prevent water on the surface from freezing.

The local dew point temperature was calculated using Engineering Equation Solver (EES) to determine the surface temperature necessary for condensation. Once condensation began, droplets were permitted to grow and coalesce with neighboring

droplets to ensure that droplets of sufficient volume were reached. The contact angle and critical sliding angles of these condensed droplets were then measured and compared with droplets injected onto the surface by micro-syringe. The volume of an individual condensed droplet was found by absorbing the droplet in high-density filter paper and then weighing it on a high-precision balance with a readability of 0.0001g to determine the droplet mass.

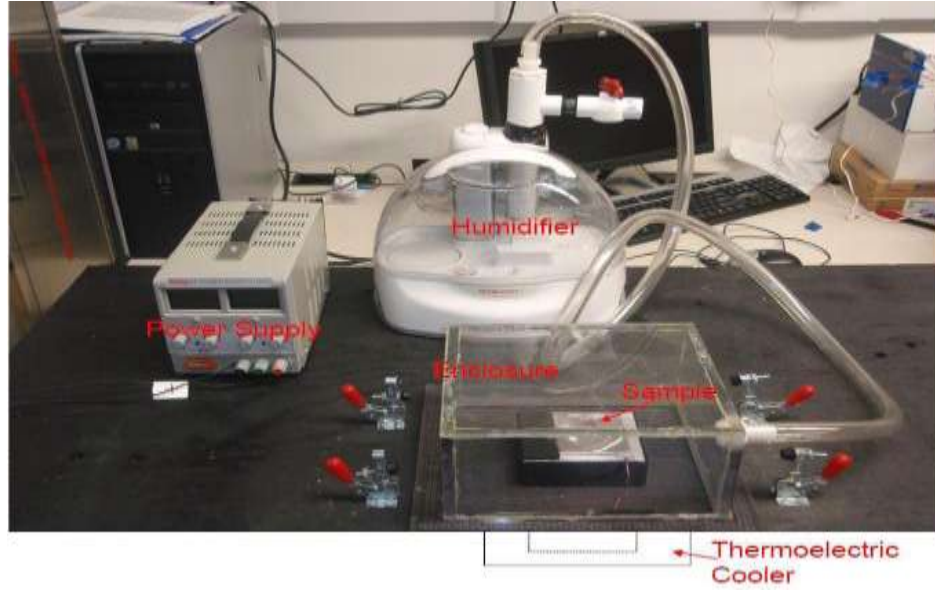


Figure 2.12 Environmentally-Controlled Condensation Chamber

2.6 Water Droplet Evaporation Rate

For most of the measurements performed in this study (i.e. contact angle, critical inclination angle, etc.), the water droplet was injected onto a solid surface. Thus, the evaporation rate of the water droplet is important in determining the accuracy of these measurements. The rate of evaporation of sessile drops was found to depend on the radius of the liquid-solid interface. The instantaneous rate of evaporation can be expressed by

$$\text{rate} = I = -\frac{dm}{dt} = -\rho\left(\frac{dV}{dt}\right) \quad (2.1)$$

where m is the mass of droplet, V is the volume and ρ is the density of water.

To calculate the rate of evaporation, small water droplets were placed on a clean aluminum surface and weighed repeatedly for 20 minutes on a digital balance with a readability of 0.0001 g. Sessile water droplets of various volumes (10 μL and 60 μL) were investigated. The plots of the resulting droplet weight as a function of time are given in Figure 2.13. These data show that the evaporation rates for droplets of 10 μL and 60 μL are 0.00026 g/min and 0.00054 g/min, respectively. This means that evaporative losses after three minutes equate to 7.8% and 2.7% for 10 μL and 60 μL droplets, respectively.

In this study, contact angle and critical inclination angle measurements were typically performed within a couple of minutes of the droplet being placed on the surface. Thus, for the range of droplet volumes examined (i.e. 5 μL to 70 μL), the effect of evaporation was not significant. Moreover, contact angle measurements have been shown to vary very little with droplet volume [35], and for the critical velocity measurements, a new droplet was injected on the surface before each test thus minimizing the effect of evaporation.

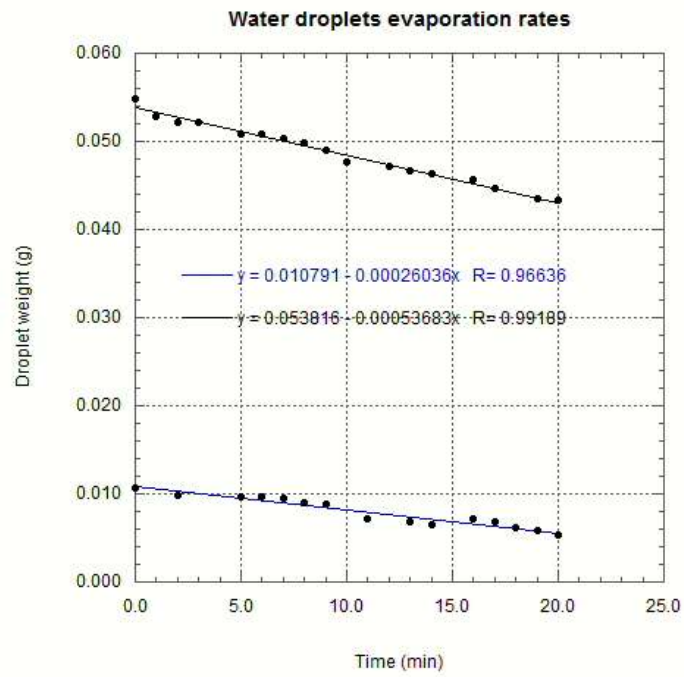


Figure 2.13 Weight of water drops (on Al surface) as a function of time. Drop weights are 0.0106g (shown in blue) and 0.000549g (black)

Chapter 3 Results and Discussion

3.1 Contact Angle Data

3.1.1 Wenzel's Model

For the experiments performed in this study, droplets were primarily observed to follow the Wenzel mode of wetting. Wenzel's model, which describes the homogeneous wetting regime, is defined by the following equation for the contact angle on a rough surface:

$$\cos \theta_r^w = \gamma \cos \theta_e \quad (3.1)$$

where θ_r^w is the apparent contact angle which corresponds to the minimum free energy for the system. The angle θ_e is the contact angle defined for an ideal, homogeneous surface (i.e. baseline surface). The roughness ratio γ is defined as the ratio of true area of the solid surface to the apparent area as shown in Figure 3.1. Thus, the roughness ratio shows how the underlying surface roughness can affect the droplet contact angle and therefore the wettability characteristics of the surface.

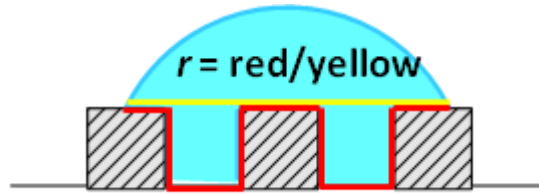


Figure 3.1 Wenzel's model

3.1.2 Advancing and Receding Contact Angle

Advancing and receding contact angles of water droplets were measured for the baseline surface, sample 1 and sample 2 under the condition of with/without PDMS coating. Sample descriptions of these test samples are shown below in Table 2.

For the baseline surface, the measured advancing contact angle was 107.1° , and the receding contact angle was 75.2° . Therefore, the contact angle hysteresis of the baseline surface was 31.9° . Contact angle hysteresis which is the absolute difference between the advancing and receding contact angles is often used as a gauge of hydrophobicity [22-26]. Reduced hysteresis usually equates to increased

hydrophobicity. As shown in Table 3, the hysteresis of the baseline Al surface only reduced slightly from 31.9° to 29.3° after applying the PDMS coating to the surface. This observation suggests that uniform modification of the surface by homogeneous chemical treatment does not necessarily alter the surface's overall wettability. By creating micro-channels on the surface, the contact angle hysteresis for Sample 1 (channel depth = 10 µm) increased to 66.0°, 70.5° and 76.1° for the 15µm, 50µm and 100µm wide channels, respectively. The addition of the micro-channels made the surface more hydrophilic (see Table 4). This observation is supported by Wenzel's model of wetting which predicts that on a naturally hydrophilic substrate, introduced surface roughness tends to make the substrate more hydrophilic.

Therefore, the treatment of the surface with a chemical coating (i.e. PDMS) was necessary. After the surface with channels was spin-coated with PDMS, the surface was found to be hydrophobic with a significantly reduced hysteresis of up to approximately 50 % (see Table 5). Another surface (Sample 2 with channel depth of 6.8µm) was also prepared and modified with micro-channels and chemical coating to study the effect of the anisotropy on the water droplet contact angle (see Table 6). It is believed, however, that the thickness of the PDMS coating mitigated the effect of the channel anisotropy on Sample 2 producing the unusual trend in hysteresis that was observed. In summary these data suggest that deeper, narrower channels affect more change in surface wettability than shallower, wider channels. (i.e. The smallest contact angle hysteresis was observed for the 15 µm wide, 10 µm deep channels on Sample 1 with PDMS coating).

Table 2: Matrix of Test Samples

<i>Sample</i>	<i>Channels (Channel Depth)</i>	<i>Coating</i>	<i>Hysteresis</i>	<i>Overall Wettability</i>
<i>Baseline Surface</i>	<i>N</i>	<i>n/a</i>	<i>32.0 °</i>	<i>Hydrophilic</i>
<i>Sample 1</i>	<i>Y (10µm)</i>	<i>PDMS</i>	<i>26.0 °</i>	<i>Hydrophobic</i>
<i>Sample 2</i>	<i>Y (6.8µm)</i>	<i>PDMS</i>	<i>34.3 °</i>	<i>Hydrophobic</i>
<i>Sample 3</i>	<i>Y (12µm)</i>	<i>n/a</i>	<i>76.1 °</i>	<i>Hydrophilic</i>

Table 3: Contact angle for baseline surface

	Advancing Angle	Receding Angle	Hysteresis
Baseline surface	107.1°	75.2°	31.9°
Baseline + PDMS Coating	119.4°	90.0°	29.3°

Table 4: Contact angle data for Sample 1 (with no coating and micro-channels 10µm deep)

	Advancing Angle	Receding Angle	Hysteresis
15µm	98.1°	32.1°	66.0°
50µm	102.2°	31.7°	70.5°
100µm	105.7°	29.6°	76.1°

Table 5: Contact angle data for Sample 1 (with PDMS and micro-channels 10µm deep)

	Advancing Angle	Receding Angle	Hysteresis
15µm	114.9°	94.3°	20.7°
50µm	116.4°	90.4°	26.0°
100µm	117.3°	87.2°	30.1°

Table 6: Contact angle data for Sample 2 (with PDMS and micro-channels 6.8µm deep)

	Advancing Angle	Receding Angle	Hysteresis
15µm	122.1°	83.7°	38.4°
50µm	122.3°	88.0°	34.3°
100µm	119.8°	91.1°	28.8°

3.2 Critical Inclination Angle Data

3.2.1 Data Analyses and Model Prediction

The so-called critical droplet refers to a droplet large enough that the surface tension retaining force is equal to the gravitational drainage force and therefore occurs at the point of incipient motion. Critical inclination angle data have been measured for the baseline surface and for the 50 µm wide channels on sample 1 and sample 2. Droplet volumes between 5 µL and 80 µL were considered and injected on the test surface using a micro-syringe. Ordinarily, the critical inclination angle scales directly with the contact angle hysteresis. Therefore, because both sample 1 and sample 2 exhibit smaller contact angle hysteresis than the baseline surface, larger critical inclination angles for sliding were expected on the baseline surface. Also, one might expect that sample 2 would have larger critical inclination angles than sample 1.

Fig. 3.2 shows representative critical inclination angle data for droplets of various sizes on these surfaces. In this figure, the baseline surface (shown in black) exhibits much higher critical inclination angles for sliding for a droplet of a given volume than the wet-etched anisotropic surfaces. With respect to sample 2 (shown in blue), the reduction in the critical inclination angle was observed to be more pronounced for larger droplet volumes, which is consistent with more of the droplet base experiencing the effect of the “micro-channels.” In other words, for small water droplets and therefore small wetted areas, the anisotropic surface effect is less pronounced. The difference in the measured critical inclination angles between sample 1 and sample 2 also suggests that sample 1 is more hydrophobic than sample 2 which agrees well with the results from the contact angle measurements. In addition, it was observed that larger critical angles of inclination were manifested by sample 1 in the perpendicular configuration as compared to the parallel configuration (see Fig. 3.3). For identical size droplets, the critical inclination angle was at least 5° larger for sample 1 in the perpendicular orientation. This shows that the channels inhibit droplet movement across the grooves while at the same time facilitating droplet movement along the channels (see Fig. 3.4).

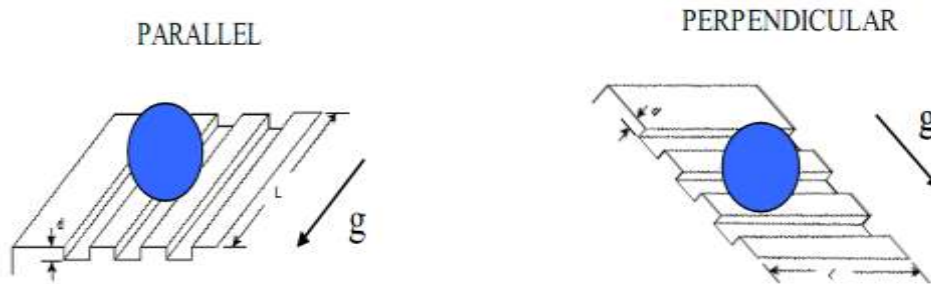


Figure 3.3 (a) Droplet moves parallel to the direction of channels; (b) Droplet moves perpendicular to the direction of channels

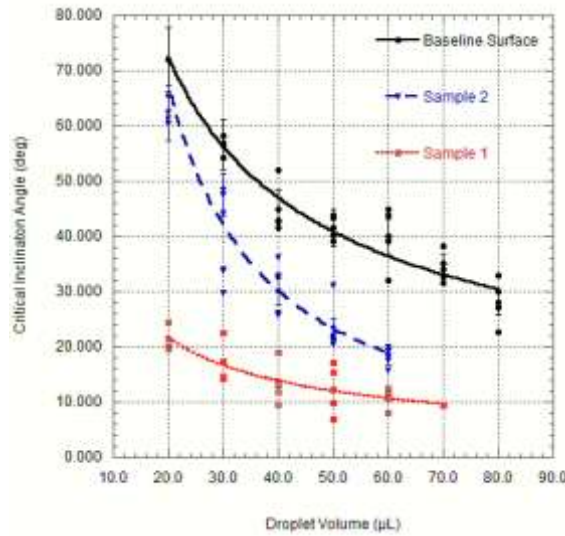


Figure 3.2: Critical inclination angle data for droplets on baseline surface, sample 1 and sample 2

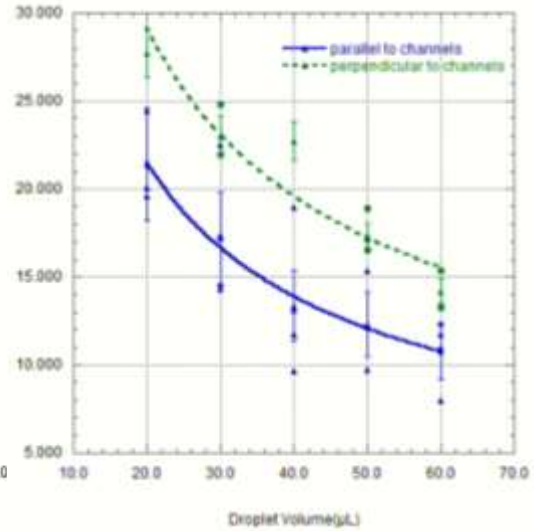


Figure 3.4: Critical inclination angle data on sample 1 for droplets moving \perp to the channels and $//$ to the channels

These data were also compared to the predicted critical droplet volume given by Dussan [27]. Using the advancing contact angle, receding contact angle, and droplet volume as inputs, the Dussan equation was utilized to predict the critical inclination angle for sliding on the baseline surface (Fig. 3.5a), sample 1 (with PDMS coating) (Fig. 3.5b) and sample 2 (with PDMS coating) (Fig. 3.5c). These data generally agreed well with the model predictions of the Dussan equation. In this analytical work, Dussan studied static droplet shapes at the critical condition on inclined surfaces where the droplet contact line possessed straight-line segments on the sides. In this view, the droplet was assumed to be elongated and parallel-sided. The most limiting restriction of this analysis is its assumption of small contact angle hysteresis. Therefore, the model may need to be modified before it can be applied to certain surfaces. This may also partially explain the deviation between the model and the data for the baseline surface which possessed moderate contact angle hysteresis.

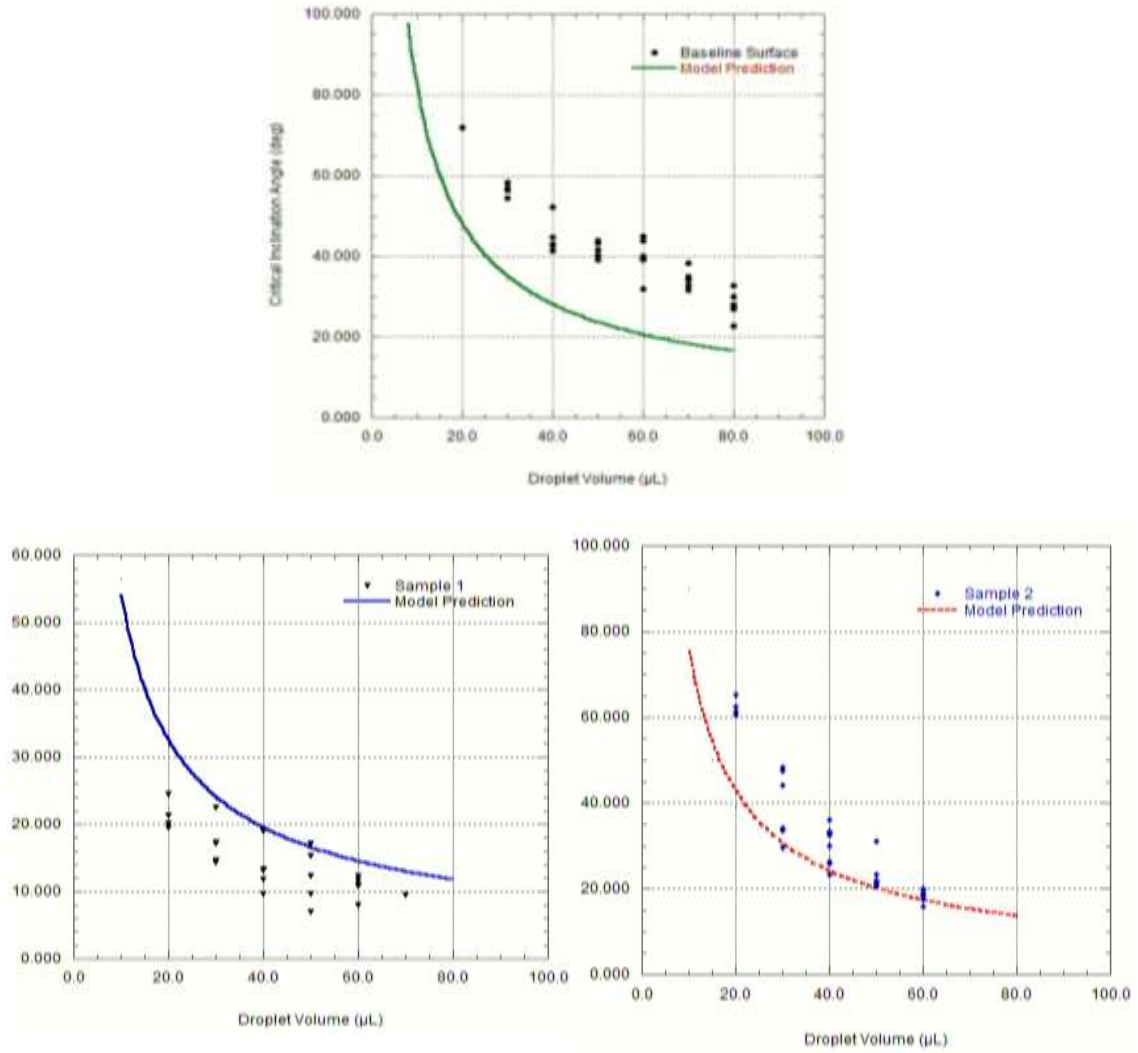


Figure 3.5: Experimental data for the (a) baseline surface, (b) sample 1, and (c) sample 2 compared with the predicted critical inclination angle using the Dussan equation [27]

3.2.2 Critical Inclination Data for Condensed Droplets

The previous critical droplet data were specifically for the case of an aluminum surface where the droplet is injected onto the surface using a micro-syringe. The condensing of water vapor onto the surface follows a mode of droplet formation much different from droplet injection. Water fills the channels first and completely wets the surface, unlike injected droplet formation, in which some or all of the channels may remain dry. These differences are highlighted in Figure 3.6 which shows both a condensed droplet and an injected droplet on Sample 1.

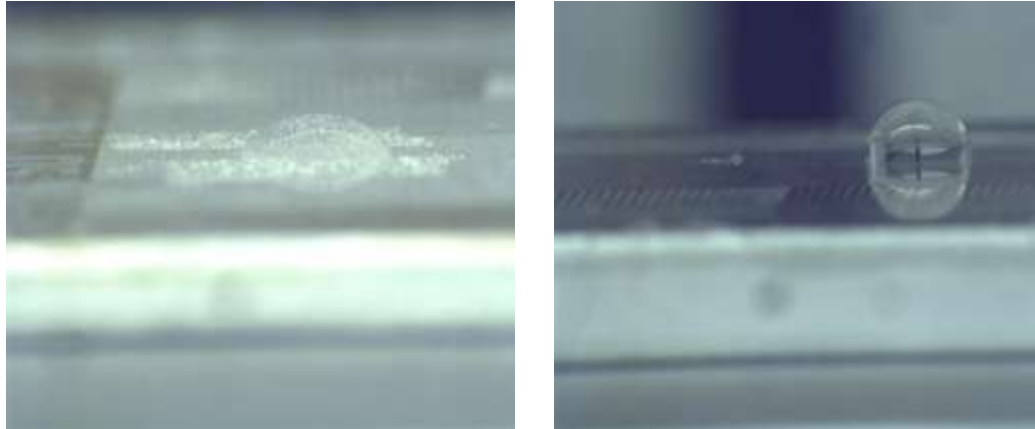


Figure 3.6 20 μL condensate droplet (left) and injected droplet (right) on Sample 1

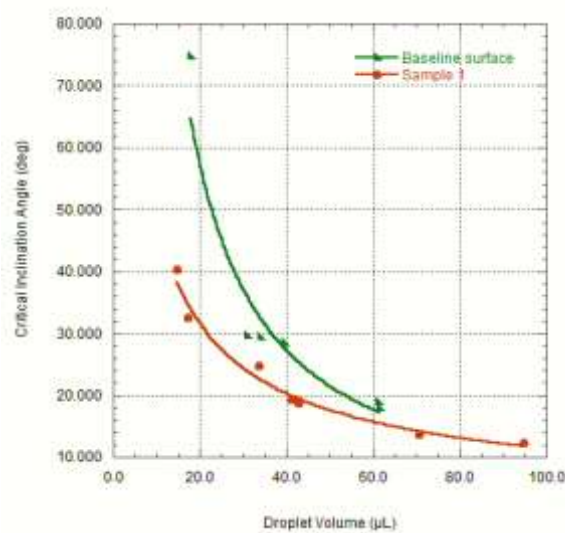


Figure 3.7: Critical inclination data for condensate droplets on the baseline surface and sample 1

Shown above in Figure 3.7 are critical inclination angle data for condensed droplets on both the baseline surface and sample 1. Similar to the injected droplet data, these condensed droplet data also suggest that sample 1 is more effective at draining water than the baseline surface—that is, water droplets condensed on sample 1 begin sliding at lower inclination angles than the baseline surface. To understand the different behavior of condensate droplets, these critical inclination angle data were then compared with the injected droplet data on various surfaces. On the baseline surface, the test results showed that the critical inclination angle is smaller for condensed droplets than injected droplets, which suggests that condensed droplets may drain

better on the baseline surface than injected droplets (see Figure 3.8). When a similar comparison was made on sample 1, as shown in Figure 3.9, the injected droplets were observed to have smaller critical inclination angles than the condensed droplets. Since condensed droplets occupy more area on the surface than injected droplets, it is hypothesized that the larger observed critical inclination angles are the result of a longer droplet contact line which would serve to increase the surface tension retaining force.

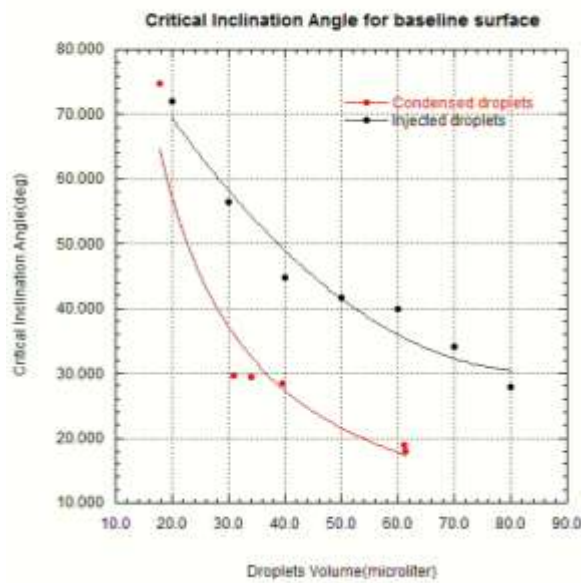


Figure 3.8 Baseline surface: inclination angle for condensate(red) and injected (black) droplets

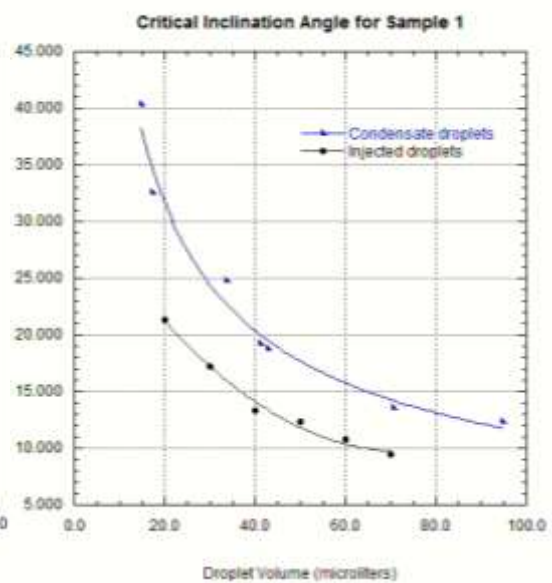


Figure 3.9 Sample 1: inclination angle for condensate(blue) and injected(black) droplets

3.3 Wind Tunnel Test Data

The tests in the wind tunnel were performed on the baseline surface, sample 1 (hydrophobic surface) and sample 3 (hydrophilic surface). Samples 1 and 3 were both prepared by etching micro-channels into the surface. Additionally, sample 1 included a PDMS surface coating while sample 3 was without such coating. The critical air-flow rate was then measured for different droplet sizes and plotted for these surfaces as shown in Fig. 3.10. Fig. 3.10a shows that the hydrophilic surface (sample

3) required larger air-flow rates for the onset of droplet motion than the baseline surface for droplet volumes between 5 and 25 μL . (i.e. The drag force required to move the droplet along the surface in the direction of the air flow is higher on sample 3 than on the baseline surface.) In other words, droplets of comparable size are less likely to be “blown off” the back side of a heat exchanger constructed using the hydrophilic aluminum as compared to the baseline case.

If the surface is processed with micro-channels and PDMS coating, as shown before, the surface is now hydrophobic (i.e. smaller contact angle hysteresis and smaller critical inclination angle). Fig. 3.10b shows that the surface with the micro-channels and PDMS coating reduces the critical air-flow force as compared to the baseline surface. Thus, a larger range of droplet sizes may be removed, and droplets condensed on the surface may be removed while they are still relatively small. Thus, large droplets which tend to increase the core pressure drop are less likely to be retained on the surface. The surface micro-structure was also observed to inhibit droplet movement across the grooves while at the same time facilitating movement along the grooves since the critical air-flow rates parallel to the channels were smaller than for droplet movement perpendicular to the channels. More specifically, the required air-flow rate for movement across the channels was 1.0-1.2 m/s larger than the air-flow rate for movement along the channels and only slightly lower than the baseline case. Depending on the application, either the hydrophilic surface (which would minimize condensate “blow-off”) or the hydrophobic surface (which would help reduce the core pressure drop by facilitating condensate drainage downwards with gravity) may be more desired. In both cases, the micro-channels provide a preferential direction and path for the water to drain.

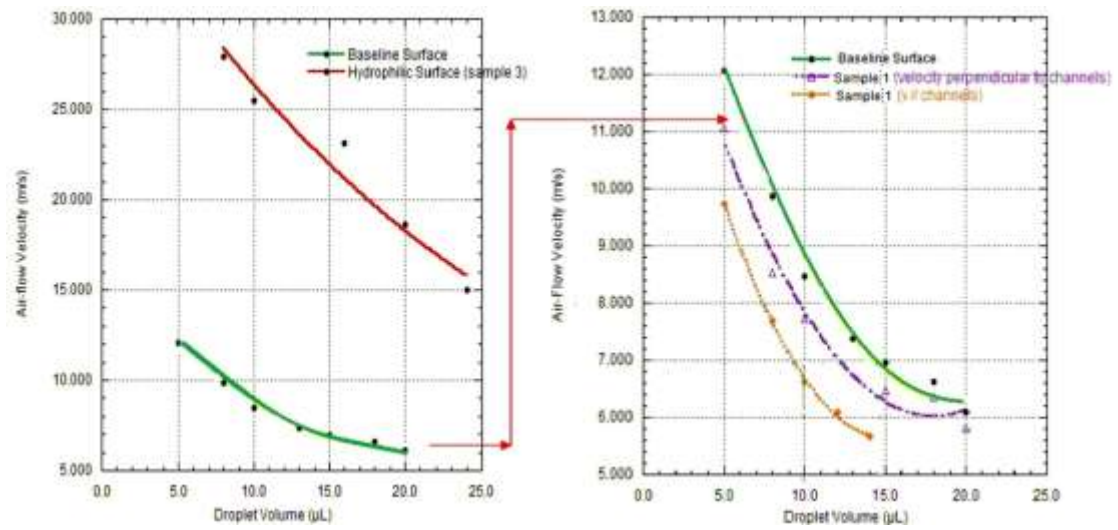


Figure 3.10: Critical air-flow rates required for droplet motion on: (a) the baseline surface and sample 3, and (b) the baseline surface and sample 1 in both the parallel and perpendicular configurations

Chapter 4 Water Droplet Modeling

4.1 Related Modeling Work

4.1.1 An Existing Model

In order to study the parameters affecting a droplet at the critical condition, a force balance may be performed on an individual droplet. A.I. El Sherbini developed an initial model for droplets at the sliding condition where the drag force was neglected, and the force balance was performed between the gravitational and surface-tension forces acting in the x - z plane (see Fig. 4.1)[28].

In this work, the surface tension force acting on the droplet in Figure 4.1 was found by integrating the differential surface tension forces around the base contour of the droplet. In this work, the droplet contour was assumed to be an ellipse with a radius, ζ , at any point described by equation (4.1):

$$\zeta(\phi) = \frac{L}{\sqrt{\cos^2\phi + \beta^2 \sin^2\phi}} \quad (4.1)$$

Thus, the surface tension force acting in the x -direction was calculated using equation (4.2):

$$F_{sx} = -2\gamma \int_0^\pi \zeta \cos\theta \cos\phi d\phi \quad (4.2)$$

where γ is the liquid surface-tension, D is the drop diameter, θ is the contact angle and ϕ is the azimuthal angle. In this model, the contact angle function $\theta(\phi)$ was written as:

$$\theta(\phi) = a_1\phi^3 + a_2\phi^2 + a_3\phi + a_4 \quad (4.3)$$

where a_1 , a_2 , a_3 , and a_4 are constants [31]. The conditions used to determine the four constants in Eq. (4.3) were:

$$\theta(0) = \theta_{\max} \quad (4.4a)$$

$$\theta(\pi) = \theta_{\min} \quad (4.4b)$$

and from symmetry, the slope of the θ function should vanish at $\phi = 0$ and 180° such that

$$\left. \frac{d\theta}{d\phi} \right|_{\phi=0} = 0 \quad (4.5a)$$

$$\left. \frac{d\theta}{d\phi} \right|_{\phi=\pi} = 0 \quad (4.5b)$$

It was also concluded that $\theta_{\max} \approx \theta_A$ for all drop sizes, surface inclinations, and

liquid–surface combinations tested. For a droplet deposited on a horizontal surface, spreading leads to a contact angle equal to θ_A . When the surface is tilted, the value of θ_{\max} cannot increase beyond θ_A . Critical θ_{\min} was almost constant and was assumed equal to the receding contact angle θ_R .

The gravitational force acting on the droplet in the x -direction can be written as:

$$F_{gx} = -\rho g V \sin \alpha \quad (4.6)$$

where α is the inclination angle of the surface. The resulting force balance on the droplet in the x -direction is then $F_{sx} + F_{gx} = 0$. This model by El Sherbini and Jacobi works well on homogeneous surfaces; however, it was never intended for use on heterogeneous surfaces such as those studied in this project. Moreover, this model does not consider the effect of the airflow force on the droplet that is commonly present in air-conditioning and refrigeration systems.

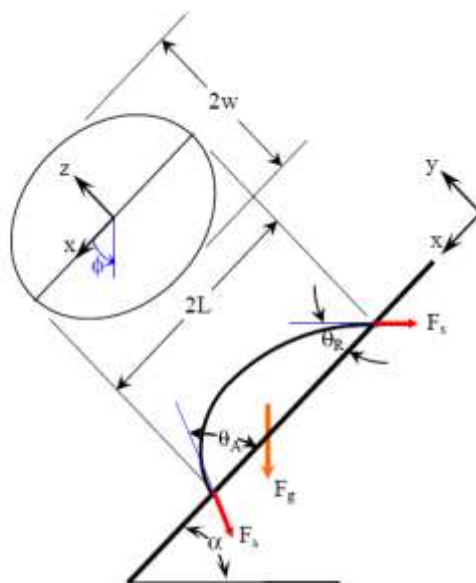


Figure 4.1: Force balance on a drop on an inclined plane with elliptical contour [28].

4.1.2 Surface Tension Force Calculation

Dussan V and Chow [20] studied static droplet shapes at the critical condition on an inclined surface for a droplet contact line with straight-line segments on the sides. In this view, the droplet was assumed to be elongated and parallel-sided (see Fig. 4.2). For

the elongated “parallel-sided” drop, the surface-tension forces at the parallel sides cancel. The contact angle was taken as the advancing angle for the lower curve of the contour and the receding angle for the upper portion. Dussan V and Chow [26] showed that for their assumption of contact angle variation described above, the retention force, F , is given by:

$$\frac{F_s}{\gamma w} = k(\cos\theta_R - \cos\theta_A) \quad (4.7)$$

where w is the drop width, γ is the liquid surface tension, and $k = 1$. The constant k is a scale factor for dimensionless retention force that depends on the assumptions for contour shape and contact angle variation. Wolfram and Faust [29] predicted a value of $k = 3.14$, while Extrand and Gent [30] predicted the k value of 1.27, which agreed with their data for small values of $(\cos\theta_R - \cos\theta_A)$. However, they under predicted retentive force at higher values of $(\cos\theta_R - \cos\theta_A)$.



Figure 4.2 Parallel-sided droplet

A.I. El Sherbini[28] suggested the form of the following equation in the x-direction to calculate surface tension force in their initial model:

$$F_{sx} = \frac{24}{\pi^3} \gamma D (\cos\theta_{\min} - \cos\theta_A) \quad (4.8)$$

This equation holds for the case where $\beta = 1$. By comparing equation (4.8) to equation (4.7), the retentive-force factor k can be obtained:

$$k = \frac{48}{\pi^3} \approx 1.548 \quad (4.9)$$

Thus, they modified equation (4.4) to be:

$$\frac{F_s}{\gamma R} = k(\cos\theta_R - \cos\theta_A) \quad (4.10)$$

where R is the radius of droplets.

4.2 Development of a New Model

4.2.1 Air Flow Force

Others have attempted to model the incipience of water droplet motion on a heat transfer surface. However, these models typically neglect the air flow force and consider only the case of water drainage on a vertical plate in the absence of air flow. In our model, the air flow force is added.

For the sliding condition on a vertical surface with the combined effects of gravity and air-flow (shown in Fig. 4.3), the critical air velocity needed for the onset of water droplet sliding is calculated using Equation 4.11:

$$F_s + F_d + F_g = 0 \quad (4.11)$$

where the air flow force is calculated as:

$$F_d = -C_d \rho_a u^2 A_{pr} \quad (4.12)$$

where C_d here is the drag coefficient, ρ_a is the density of air, u is the air-flow velocity and A_{pr} is the projected area of the droplet.

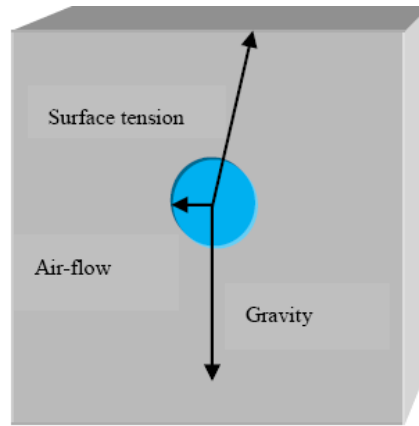


Figure 4.3 Force balance on a vertical surface with air flow

4.2.2 Droplet Projected Area

A liquid droplet on a horizontal plane takes the shape of a hemispherical cap. In this case, the projected area A_{pr} may be approximated as:

$$A_{pr} = \frac{D^2 \theta_M}{4} - \frac{D^2 \cos \theta_M \sin \theta_M}{4} \quad (4.13)$$

$$\theta_M = \frac{\theta_A + \theta_R}{2} \quad (4.14)$$

where θ_A is advancing contact angle and θ_R is receding contact angle. However, when the surface is tilted, the surface of the droplet becomes “elongated” due to gravitational forces and the droplet shape changes. Because the droplet can no longer be treated as a hemispherical cap and is even less hemispherical on the modified surface, a “two-circle method” was adopted to predict the projected area of the droplet (see Fig. 4.4) using an approach similar to the one presented in [22]. In this approach, the droplet periphery is fitted with two circles instead of one to better represent the contour of the droplet.

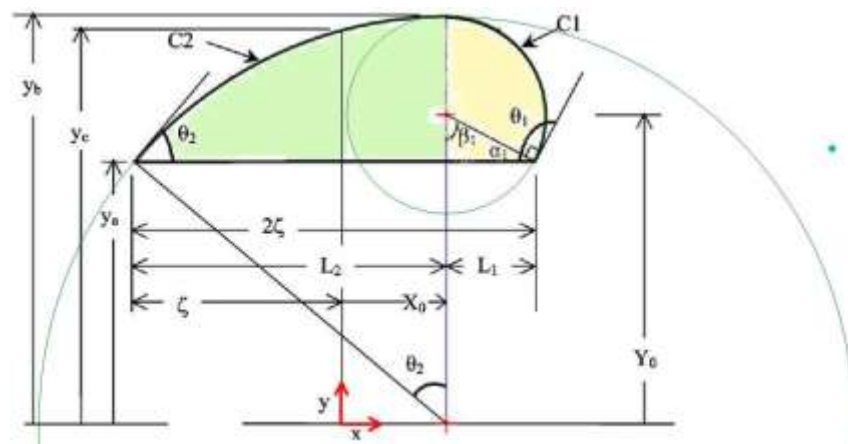


Figure 4.4: Schematic of the “two-circle” method [26]

Using this method, the following equations (4.15)-(4.19) were derived to calculate the projected area:

$$L_f = \frac{\sin\theta_1 (1-\cos\theta_2)}{\sin\theta_2 (1-\cos\theta_1)} \quad (4.15)$$

$$L_1 = \frac{DL_f}{1+L_f} \quad (4.16)$$

$$L_2 = \frac{D}{1+L_f} \quad (4.17)$$

$$\beta_1 = \pi - \theta_1 \quad (4.18)$$

$$A_{pr} = \pi \frac{L_1^2}{(\sin\theta_1)^2} \frac{\theta_1}{2\pi} - \frac{1}{2} L_1 \frac{L_1}{\tan\theta_1} + \pi \frac{L_2^2}{(\sin\theta_2)^2} \frac{\theta_2}{2\pi} - \frac{1}{2} L_2 \frac{L_2}{\tan\theta_2} \quad \theta_1 < 90^\circ, \quad \theta_2 < 90^\circ$$

$$A_{pr} = \pi \frac{L_1^2}{(\sin\beta_1)^2} \frac{\theta_1}{2\pi} + \frac{1}{2} L_1 \frac{L_1}{\tan\beta_1} + \pi \frac{L_2^2}{(\sin\theta_2)^2} \frac{\theta_2}{2\pi} - \frac{1}{2} L_2 \frac{L_2}{\tan\theta_2} \quad \theta_1 > 90^\circ, \quad \theta_2 < 90^\circ \quad (4.19)$$

where θ_1 is the advancing contact angle and θ_2 is the receding contact angle.

Due to the difference in the advancing and receding contact angles, using two circles provides a more accurate prediction of the droplet projected area for use in the

model. For the baseline surface, it can be shown that the two-circle method predicts 4% more projected area than the one-circle method, whereas for the modified surface, the two-circle method covers about 3% less projected area than the one-circle method.

4.2.3 Droplet Diameter vs. Droplet Volume

In order to create a model of droplet behavior on a surface at the sliding condition, an accurate knowledge of the droplet diameter is needed. On a horizontal surface, water droplets take the approximate shape of a spherical cap, where the contact line is circular and the contact angle is constant. In this case, the volume may be expressed as a function of diameter such that:

$$V = \frac{\pi D^3}{24} \left(\frac{2 - 3\cos\theta + \cos^3\theta}{\sin^3\theta} \right) \quad (4.20)$$

where θ is the apparent contact angle [22]. The profile of the drop appears as part of a circle as shown in Fig. 4.5. On a tilted surface, researchers have relied on the assumption of an elliptical base contour shape to determine the droplet diameter as a function of the droplet volume. Although this approach usually works well on homogeneous surfaces, this assumption does not necessarily hold on anisotropic surfaces such as those studied in this work where unusual droplet base contour shapes are often manifest and significant droplet elongation is present.

To measure the diameter of the droplet, a Ramé-Hart precision contact angle goniometer was used to image the droplet. The major axis diameter was then measured using standard image processing software. A representative side image of a droplet on a vertical surface is shown in Fig. 4.6. Since the droplet volume was known *a priori* using the micro-syringe, an equation relating the droplet diameter to the droplet volume could be determined. To derive these relationships, experimental data from different surfaces were used as shown in Equations (4.23) and (4.24):

$$D = 1.6553 \times V^{0.2906} \quad \text{Baseline Surface} \quad (4.23)$$

$$D = 0.9804 \times V^{0.4967} \quad \text{Sample 1 (with channels and PDMS)} \quad (4.24)$$

where V is the droplet volume (μL) and D is the droplet diameter (mm). From these relationships, it is apparent that droplet spreading (i.e. larger D) is more pronounced on the baseline surface for small droplets than on sample 1 which is hydrophobic. Comparing Eq. 4.20 with Eq. 4.23, it can be shown that the diameter of a droplet on vertical surfaces (see Fig 4.7). Eq.4.24 was also applied for modeling droplet behavior on sample 2 and sample 3.

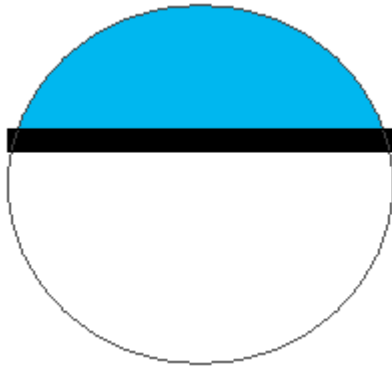


Figure 4.5 Profile of droplets fits a circle. Figure 4.6 Side image of a droplet on a vertical baseline surface

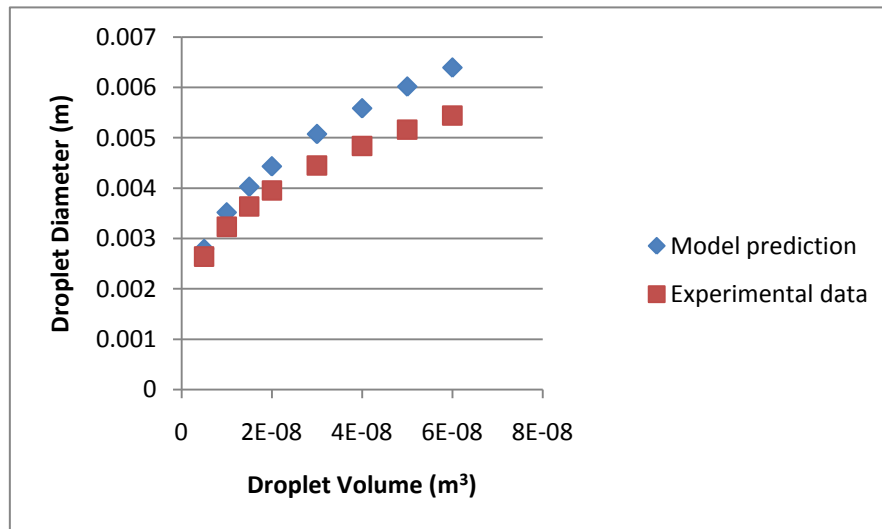


Figure 4.7 Droplet volume (m^3)(x-axis) vs. droplet diameter (m)(y-axis):data points shown in blue assumed a circular contact line; experimental data on a vertical surface are shown in red

4.2.4 Drag Coefficient

Another thing which has been improved in the current model is the drag

coefficient, C_D . Past researchers have relied on the experiments by Al-Hayes and Winterton for bubbles detaching from a solid surface in flowing liquids [32]. In this work, the equilibrium contact angle ranged from 22 ° and 90 °, and the drag coefficient was found to be:

$$\begin{aligned} C_D &= 1.22 & \text{for } 20 < \text{Re} < 400 \\ C_D &= 24 / \text{Re} & \text{for } 4 < \text{Re} < 20 \end{aligned} \quad (4.25)$$

where the Reynolds number was defined as:

$$\text{Re} = \frac{\rho_a u D}{\mu} \quad (4.26)$$

where μ is the dynamic viscosity of air and ρ_a , u and D are the same as defined earlier. In this project, the calculated Reynolds number ranged from 1500 to 2500. Since these Reynolds numbers exceed 400, the drag coefficient reported in Al-Hayes and Winterton could not be used. (Note: In Al-Hayes and Winterton's experiments, u was defined as the local boundary-layer velocity at the droplet half-height and a location midway across the surface. In these experiments, the velocity was taken equal to the mainstream velocity since the boundary layer is thin and according to the Blasius velocity profile, the local velocity at the droplet half-height is within 99.9% of the mainstream velocity.)

In order to find the drag coefficient for $1500 < \text{Re} < 2500$, the critical air-flow velocity for droplet movement was measured on a flat horizontal plate in the wind tunnel (see Fig. 4.8). At the incipience of droplet motion, the surface tension force should equal the air flow force. That is, the forces on the droplet should satisfy the equation $F_s + F_d = 0$. Thus, in the case where the surface tension force is well known, the drag coefficient can be estimated fairly accurately using this method. For these experiments, a baseline surface (no channels, no coating) was used. By examining a horizontal surface, the effect of gravity could be neglected.

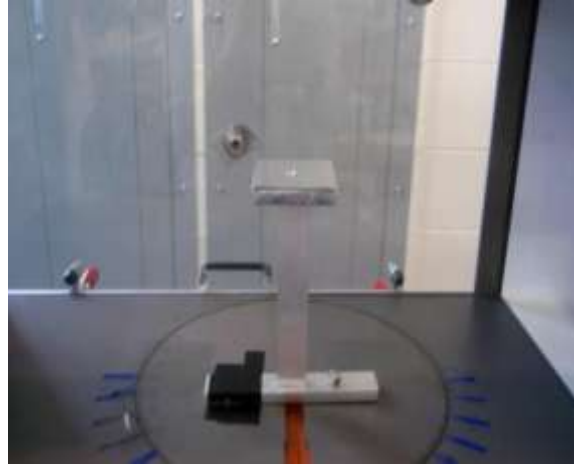


Figure 4.8 A horizontal surface in wind tunnel

After the critical air-flow velocity u was measured in the wind tunnel, the Reynolds number was calculated from Eq. 4.26. The apparent contact angle for this flat baseline surface was 84.9° , and the droplet diameter was calculated using Eq. 4.20. Values for the droplet volume, air-flow velocity and Reynolds number are shown below in Table 8 for a horizontal baseline surface at this critical condition.

At each of these recorded conditions, force balance equality between the surface tension and air-flow force was used to measure the drag coefficient. In this method, the critical air velocity, droplet volume, and droplet contact angles are specified as inputs (see Appendix A). Each of these conditions produced a slightly different drag coefficient. These values were averaged, and the average value for the drag coefficient was then used in the final model for droplet shedding on a vertical fin surface. Using this method, the drag coefficient C_D was found to be 0.4461.

Table 7 Droplet Volume, “Blow-Off” Velocity, Reynolds Number for the Baseline and C_d

Volume(μ l)	Velocity(m/s)	Reynolds Number	Drag Coefficient
10	10.07	2330	0.4632
15	9.79	2593	0.4281
20	9.08	2647	0.4522
30	8.74	2916	0.4264
40	8.14	2989	0.4466
50	7.83	3098	0.448
60	7.51	3157	0.4583

4.2.5 Surface Tension Force

(1) On a horizontal baseline surface

The calculation of the surface tension force at the sliding condition is made by performing the integration:

$$F_{sx} = -A\gamma \int_0^{2\pi} \zeta \cos\theta \cos\phi d\phi \quad (4.27)$$

which incorporates the scaling factor A from the drag coefficient calculations performed on the horizontal surface. This scaling factor ($A=1.285$) which was shown to better describe the surface tension force on the baseline surface is used for all surfaces. It does not represent a floating tuning parameter but rather a fixed parameter which was determined once using experimental data from the baseline surface. The inclusion of this factor implies that a 28.5% under-prediction of the surface tension force would result if Eq. 4.2 was used instead. .

Eq.4.10 could also be used for calculating the surface tension force on a horizontal base line Al surface; however, the value of k would no longer be 1.548.

(2) On a vertical baseline Al surface

When a droplet on a vertical surface experiencing a cross flow of air reaches the critical condition, it will slide at an angle ϕ with respect to the vertical. This force balance condition shown in Fig. 4.3 is different from the droplet force balance experienced on the horizontal surface.

Previously, Eq. 4.27 was adopted which assumes that the droplet is symmetric around the center plane. However, with the addition of the air-flow force, the droplet changes shape and moves along the surface at an angle ϕ with respect to its original position. Thus, to calculate the surface tension force on a vertical surface with both the air flow force and gravity, a modification should be made to Eq.4.27:

$$F_{sx} = -A\gamma \int_0^{2\pi} \zeta \cos\theta \cos(\phi - \phi) d\phi \quad (4.28)$$

The angle ϕ is inserted here to take into account the fact that the droplet slides on the vertical surface at an angle. Without the angle ϕ , the surface tension force is aligned up

and down and not along the direction of movement. This modification is necessary to properly resolve the surface tension force along the line of water droplet movement. Using the above equation, the corresponding k value for use in Eq. 4.10 can also be found.

4.2.6 Angle of Movement on a Vertical Surface

For the sliding condition on a vertical surface with the combined effect of gravity and air flow, surface tension acts against the movement caused by these two forces. As a result, droplets on a vertical surface will slide at an angle with respect to the vertical.

(1) Experiment Methods:

These experiments were conducted using the wind tunnel and a high-resolution CCD camera with a tripod which was placed at a fixed location from the test section of wind tunnel (see Figure 4.9). After a water droplet of known volume was injected onto the sample by micro-syringe, a picture was taken and saved to record the initial position of the droplet. Next, the blower was activated, and the droplet was checked for motion along the surface. If droplet motion was not immediately observed, the fan was turned “off”, a new droplet was placed on the sample, and the fan speed was incrementally increased using a PID controller. A picture of the new droplet was also taken using the CCD camera. When droplet motion was first detected, several pictures of the droplets sliding on the surface were taken using the CCD camera which was connected to a laptop. These images were then analyzed using standard image processing software to find the angle ϕ (see Figure 4.10).



Figure 4.9 Equipment used for angle measurement: wind tunnel, CCD camera, tripod, light source and a laptop

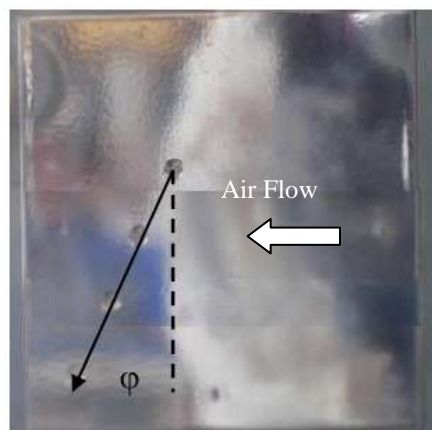


Figure 4.10: Track of a droplet on vertical surface with air-flow from right to left

(2) Data analysis:

For a droplet of known volume, at least five images were taken after the droplet started to move. Experiments were performed for droplet volumes of 5, 8, 10, 13, 15 and 18 μL . Droplets with same volume were also placed on at least three different locations on the surface. The angles calculated for these different locations on the surface were then averaged before determining the final empirical relationship between the droplet volume and the sliding angle.

To find the sliding angle ϕ of a droplet with respect to vertical, an image of the droplet's initial position was needed (see Fig. 4.11a). The images which were taken after the droplet was first observed to start moving were then compared with the initial image to find the angle (see Fig. 4.11b). ADOBE Photoshop CS4 Extend was used for processing these images.



Figure 4.11a Droplet image at $t=0$

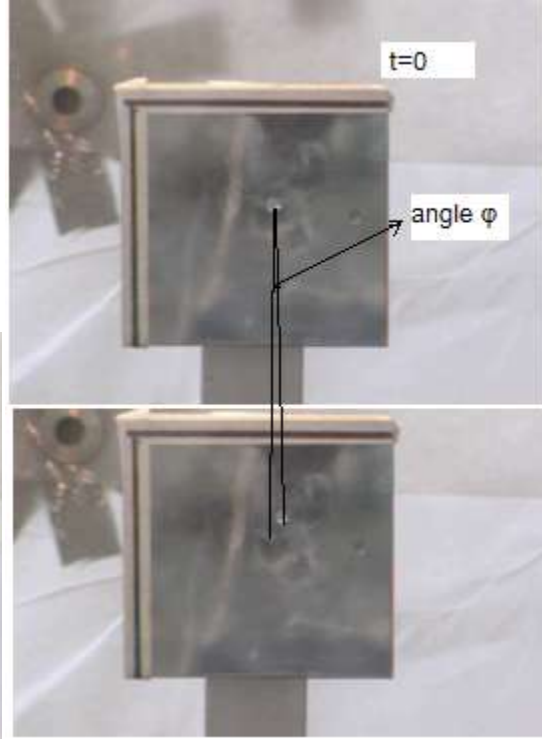


Figure 4.11b Droplet images after sliding

The results of the average sliding angle are shown below in Table 8. Based on these data, the angle ϕ was observed to follow the following equation for droplets between 5 μL and 25 μL in size:

$$\phi = 0.0035V^5 - 0.195V^4 + 4.1084V^3 - 40.711V^2 + 186.95V - 292.94 \quad (4.29)$$

where V is the droplet volume (μL).

Table 8: Angle of Movement on a Vertical Baseline Surface

Volume(μL)	Angle with vertical: ϕ
5	26.7°
8	17.3°
10	15.9°
13	21.3°
15	19°
18	24.9°

4.2.7 Surface Tension Force on Anisotropic Surfaces:

Almost all of these initial modeling efforts were focused on the baseline surface. However, the overall objective of these efforts was to create a general model that could be applied to other anisotropic fin surface designs. By allowing a few input parameters to the model such as the surface contact angles to be changed, it was hoped that a general model could be created which would enable the user to study various modified surfaces having an underlying surface roughness and/or chemical coating. The equation typically used to calculate the surface retentive force is to integrate the local surface tension force along the contact line (see Equation 4.28). For a surface with channels, the contact line may be broken and vary in length at different locations on the surface (Cassie mode of wetting). Alternatively, the length of the contact line may be increased due to additional contact within the channels (Wenzel mode of wetting). This can add considerable complexity and uncertainty to the model for surfaces with micro-channels since accurate modeling of the contact line is imperative for accurate calculation of the surface tension force. For this reason, it was believed that Equation 4.10 would be more suitable for calculating the surface tension force. For homogeneous surfaces such as the baseline surface, various k values have been reported in the literature. This research also attempted briefly to calculate the k value experimentally. Using this approach, the k value represents a simple surface parameter that can be scaled with the geometry of the surface (i.e. channels, posts, etc.) and thus account for surfaces of different roughness.

In the case of parallel micro-channels,, one possibility that eliminates the need for multiple k values would be to introduce a factor into the model that accounts for these changes in the underlying surface roughness (see Fig. 4.12). For example, for a micro-structured surface exhibiting Wenzel's mode of wetting with channels of width w_1 and depth d , the ratio of the contact line length on this surface to the original contact line length on the baseline surface would be:

$$\psi = \frac{w_1 + 2d + w_2}{w_1 + w_2} \quad (4.30)$$

In the case where $w_1 = w_2$, this expression simplifies to:

$$\psi = \frac{w+d}{w} \quad (4.31)$$

In this approach, the surface tension force would be calculated using the following expression:

$$\frac{F_s}{\gamma R} = k \cdot \psi \cdot (\cos\theta_R - \cos\theta_A) \quad (4.32)$$

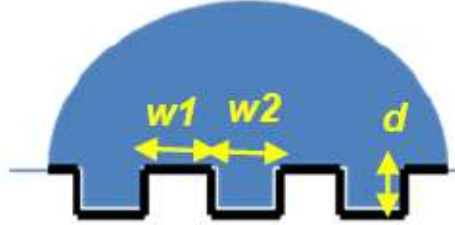


Figure 4.12 A substrate of high surface energy satisfying Wenzel's mode of wetting

4.3 Results and Conclusion

For water droplets on a vertical surface such as water condensed on the Al fins of heat-exchangers, the final expressions for the forces acting on the droplet are shown below (see Fig. 4.3):

$$\text{Air flow force: } F_d = -C_d \rho_a u^2 A_{pr} \quad (4.33a)$$

where $C_d = 0.4461$ and the projected area is calculated using the two-circle method,

$$\text{Gravitational force: } F_{gx} = -\rho g V \sin\alpha, \text{ and} \quad (4.33b)$$

$$\text{Surface tension force: } F_{sx} = -A\gamma\psi \int_0^{2\pi} \zeta \cos\theta \cos(\theta - \varphi) d\theta \quad (4.33c)$$

where $A=1.285$. Alternatively, surfaces tension force on baseline surface can be calculated using the equation below:

$$\frac{F_s}{\gamma R} = k \cdot \psi \cdot (\cos\theta_R - \cos\theta_A) \quad (4.33d)$$

where $\psi = \frac{w_1+2d+w_2}{w_1+w_2}$ and $k=1.96$.

At the critical condition (i.e. incipient droplet motion), the following condition must be satisfied:

$$\text{Force balance: } F_s + F_d + F_g = 0 \quad (4.33e)$$

User Inputs to the model: Droplet volume V , advancing contact angle θ_A , receding contact angle θ_R , and ψ

Output of the model: Critical air-flow velocity, u

4.3.1 Model Predictions on a Vertical Baseline Surface

For the baseline surface (i.e. $\theta_A = 107.1^\circ$, $\theta_R = 75.2^\circ$, $\psi = 1$), the model was tested for the volume range from 5 to 15 μL . The results are shown below in Fig. 4.13 with respect to the experimental data.

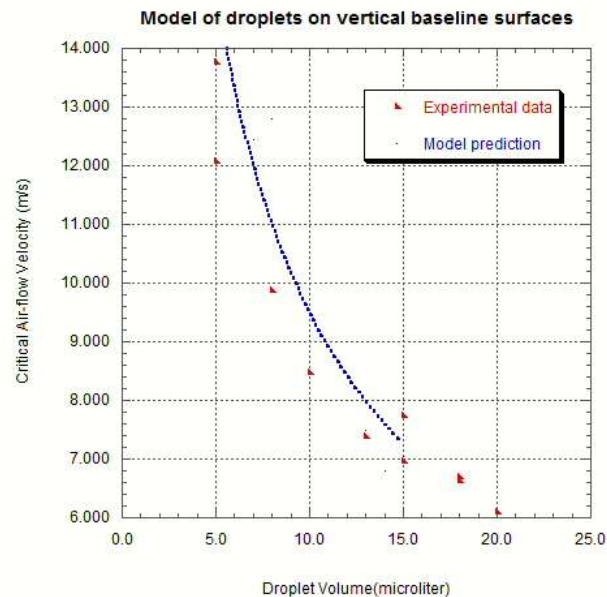


Figure 4.13 Model prediction of the critical air-flow velocity (blue curve) and experimental data (red)

The model is observed to predict the trends of experimental data rather well. The largest differences occurred at low velocities (i.e. < 3 m/s). Since it is a general model for studying droplets behavior on various aluminum surfaces with relatively few inputs, the accuracy of the model was therefore somewhat reduced. The main utility of the model, however, is that it allows the user to predict the apparent behavior of droplets on various surfaces and thus may be useful in the design and construction of future heat exchanger fins.

4.3.2 Droplet Behavior on a Vertical Anisotropic Surface

Next, the model was applied to a few different anisotropic surfaces—namely, Sample 1, Sample 2, and Sample 3.

Sample 1 contains micro-channels (channel depth = 10 μm) and a PDMS coating and has advancing and receding contact angles of 116.4° and 90.4°, respectively. For the nominally 50 μm wide channels, considering the etching process and channel depth, $\psi = 1.2$ (i.e. $w_1 = 40\mu\text{m}$, $w_2 = 60\mu\text{m}$ and $d = 10\mu\text{m}$). Figure 4.14 shows the model predictions for sample 1 with respect to the experimental data together with the results from the baseline surface. These results show that the model works better for baseline surface. It is mainly because the model was built based on the data taken from baseline surface. For anisotropic surfaces, in the model, the inputs of contact angles were intended to capture the effect of the chemical surface coating such as PDMS. Similarly, the parameter ψ was used to describe the topographical microstructure of the surface. However, ψ is only a dimensionless factor which was taken by observing the channels from one side. This two-dimensional representation is admittedly an over-simplified means of reproducing the contact line of the droplet on these surfaces. . It is believe that this model could be improved if a more detailed description of droplet wetting on these surfaces was available. However, these attempts to model anisotropic surfaces are still useful for general research of surface wettability since the model correctly shows that sample 1 is more hydrophobic than the baseline surface using only a few input parameters to represent the surface. Those parameters, the dynamic contact angles and ψ , thus play an important role in defining the wettability of the surface.

Sample 2 has micro-channels (channel depth = 6.8 μm) and PDMS coating and has advancing and receding contact angles of 122.3° and 88°, respectively. For this surface, the value of ψ for the “50 μm wide” channels is only a function of etching depth d —namely, $\psi = 1.136$. The model predictions for sample 2 are shown in Fig. 4.15. The experimental data of sample 1 are also shown in the plot. As discussed earlier, sample 1 is more hydrophobic than sample 2; however, sample 2 requires smaller air-flow velocities for droplet removal. One explanation is that when droplets

are pushed by the air to move across the channels, they can move more freely on the surface of sample 2 because the channels are shallower.

Sample 3 also has micro channels (channel depth = 12 μm) but no chemical coating. For this surface, the advancing and receding contact angles are 102.2° and 31.7°. For the “50 μm wide” channels: $\psi = 1.24$ (i.e. $w_1 = 36 \mu\text{m}$, $w_2 = 64 \mu\text{m}$ and $d = 12\mu\text{m}$). Without any chemical coatings, the wettability of sample 3 was only modified by the surface roughness. In the model, the contact angles and ψ were determined by surface roughness and the structure of channels. The predictions provided by the model agreed relatively well with the experimental data (see Fig. 4.16). Also encouraging, these model predictions show sample 3 to be hydrophilic as compared to sample 1 and sample 2 (see Fig. 4.17) which agrees well with the earlier data shown in Fig. 3.9a.

By applying the model to sample 1, sample 2 and sample 3 and comparing the results with experimental data, it can be concluded that this model is fairly robust and useful for predicting trends associated with the wettability of aluminum fin surfaces.. Using a few simple parameters such as contact angles as inputs, this model can predict changes in surface wettability due to both physical and chemical modification. The model also highlights the advantages of the anisotropic surface structure and thus can be used as a tool in the design of future micro-channel surface geometries.

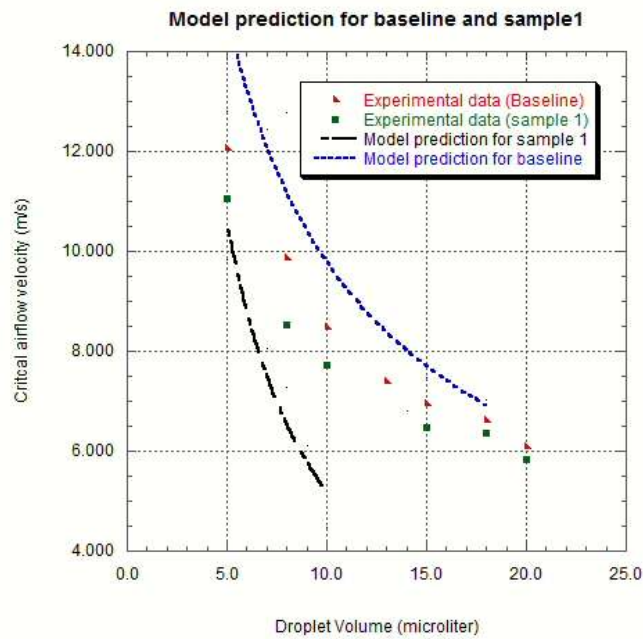


Figure 4.14 Model prediction for baseline (blue curve), Sample 1 (black curve) and their experimental data

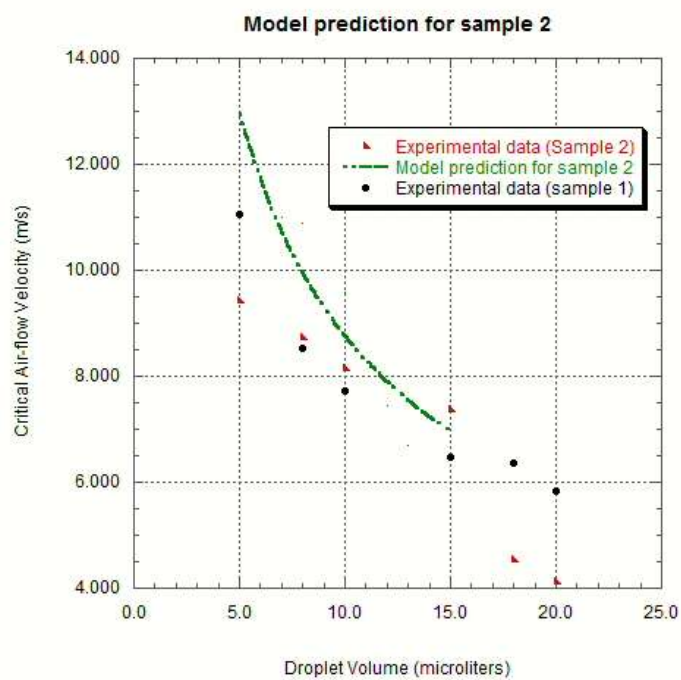


Figure 4.15 Model prediction for sample 2 (green curve) and experimental data of sample 2 and sample 1

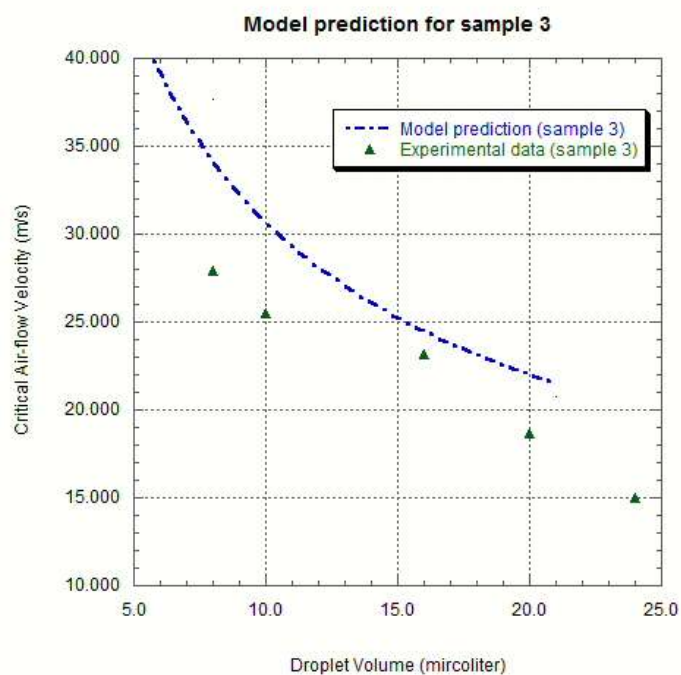


Figure 4.16 Model prediction for sample 3 (blue curve) and experimental data (green curve)

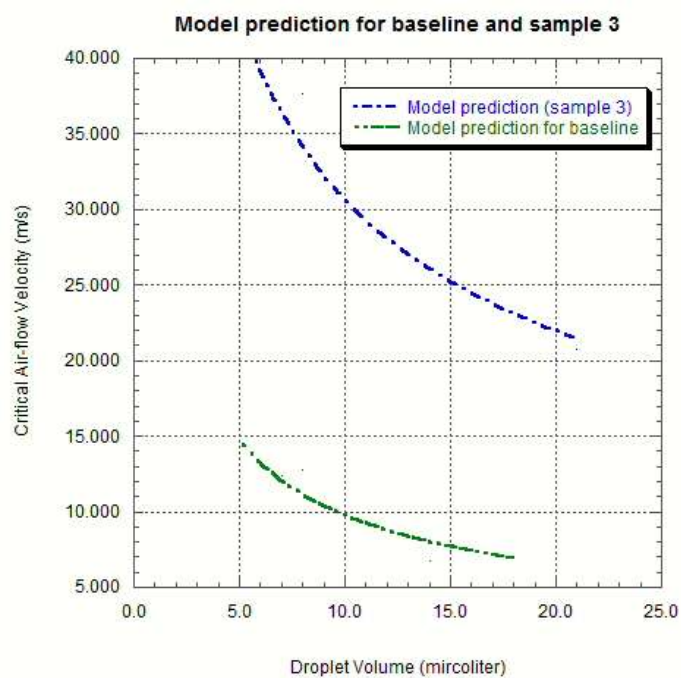


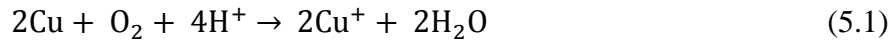
Figure 4.17 Model prediction for sample 3 (blue curve) and baseline surface (green curve)

Chapter 5 Manufacturing Surfaces with Chemical Stripes

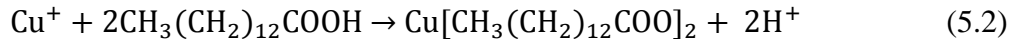
5.1 Literature Review

Several different methods have been reported in the literature for making super-hydrophobic surfaces. Most of these techniques, however, have focused on silicon substrates, not metals.

Wang et al. presented a simple electrochemical deposition process to make a super-hydrophobic surface on copper plates [34]. In this study, Wang et al. successfully fabricated a novel super-hydrophobic surface by simply immersing a copper plate (or any substrate coated with copper) into a solution of *n*-tetradecanoic acid at ambient temperature. The *n*-tetradecanoic acid was diluted into ethanol to provide an acidic environment for copper oxidization. The spontaneous oxidation reaction of copper was accelerated drastically:



In the solution, the released copper ions were then captured by *n*-tetradecanoic acid to form copper carboxylate:



The flower-like clusters of $\text{Cu}(\text{CH}_3(\text{CH}_2)_{12}\text{COO})_2$ formed on the surface after immersing for about 5 days were found to have a high water contact angle of about 162° and a sliding angle of 2° . It was also reported that this method can be applied to different metals such as aluminum. Thus, this simple method was also studied in this research as an alternative way for anisotropic wettability surface manufacturing.

5.2 Experimental Methods

The advantages of this method are: (1) it requires relatively few steps to create super-hydrophobic surfaces which are important for industrial applications, and (2) it does not need any farther chemical coatings to modify the surface. These two improvements are important for real manufacturing processes and thus the potential utilization of the process in commercial HVAC&R applications. Super-hydrophobic,

self-cleaning surface can be used to make heat exchangers which require both good thermal conductivity and environmental stability. The stability of the surfaces produced by Wang et al was tested by immersing them in a variety of chemicals like acids, bases, acetone, ethanol and toluene. No significant changes with respect to the contact angles [34] were reported. The new process can offer a huge improvement over the earlier approach based on hydrophobic polymers such as PDMS, which may reduce the thermal conductivity of the fin and may not be able to stand for a long time in the environment.

However, as reported, the result of this method varied significantly with both the concentration of the solution and the immersion time. The ideal concentration was found to be 0.01 M (*n*-tetradecanoic acid), and the immersion time was at least two days to increase the contact angle to 130°.

Therefore, one of the goals of this research was to study the effect of the concentration of the solution on the wettability of the surface in hopes of shortening the experimental time.

5.2.1 Electro Deposition Process

Initially, to accelerate the chemical reactions in the solution, an electro deposition process was used and the solution concentration was increased. During the process, two copper plates were placed in the solution and connected to a 6 V battery. The distance between them was approximately 2 - 3cm (see Fig 5.1). The plate connected to the negative terminal is herein referred to as the working electrode. This process accelerates the copper oxidation process and creates the copper carboxylate structures more quickly. Our idea was to build upon this process in order to fabricate alternating micro-scale channels of hydrophilic/hydrophobic properties. The hydrophilic channels would be bare Al or Cu and will thus provide good thermal conduction, and the hydrophobic copper carboxylate channels will facilitate droplet drainage along the channels. Yet, the results of Wang et al are reproduced first.

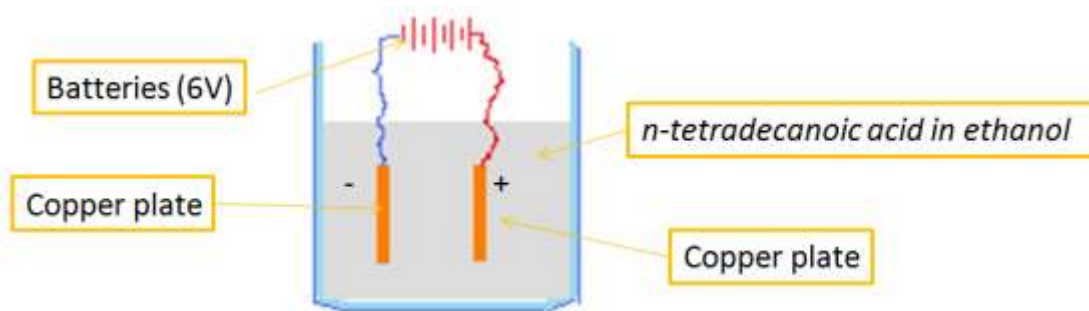


Figure 5.1 Electro-deposition processes

The basic experimental steps are as follows:

1. Sample preparation:
 - (1) Clean the copper plate with ultrasonic bath for 10 minutes
 - (2) Clean the surface with scientific grade detergent Alconox for 15 minutes, then rinse thoroughly in water
 - (3) Clean in acetone and isopropyl alcohol (IPA)
 - (4) Prepare 0.02 M *n*- tetradecanoic solution
2. Connect with the battery and immerse the samples in the solution of *n*-tetradecanoic acid for electro deposition.
3. Clean the surface with water and ethanol

After 3 hours immersed in 0.02 M solution, the copper plate was found to have a contact angle of 132° (see Fig. 5.2). Flower-like clusters were also observed on the surface (see Fig.5.3) when imaging with an FESEM. By using the process of electrodeposition, the reaction time was reduced to 3 hours; however, the copper carboxylate micro-clusters were also found to prefer to form in the solution rather than on the copper plates. From the “charging effect” during SEM imaging, it is concluded that the copper carboxylate surface is significantly less conductive than straight copper metal.

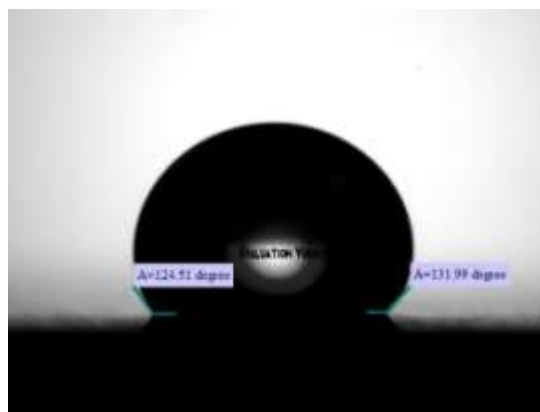


Figure 5.2 A droplet on the copper surface: apparent contact angle 131.9°

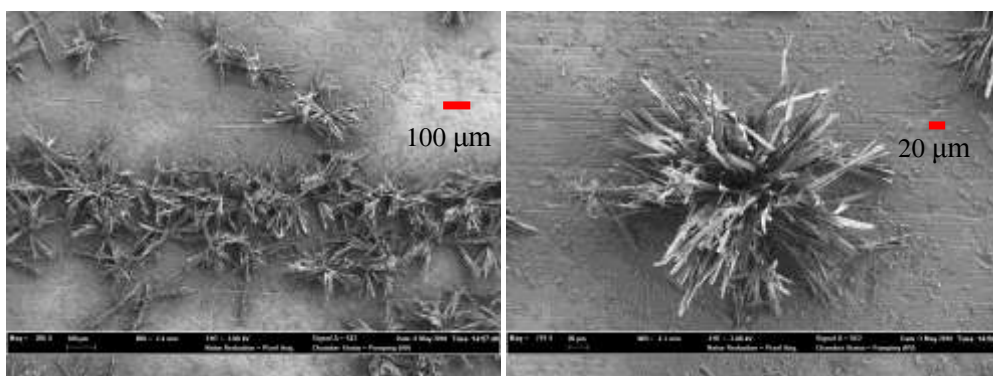


Figure 5.3 SEM images of flower-like clusters on copper surface

5.2.2 Thermal Stability Test

Thermal stability is an important parameter for a surface used in HVAC&R systems. To test the thermal stability of these surfaces containing the copper carboxylate structures, a sample was baked for 10 minutes at 100°C on a hot plate. The sample was then left to cool to room temperature following which contact angle measurements and SEM images of the surface were taken. The contact angle changed to 108 degree (see Fig. 5.4). Although the surface may still be considered as hydrophobic, the surface wettability was changed significantly suggesting that the thermal stability of these structures is fairly low at elevated temperatures. The SEM images of the clusters also show significant changes in the appearance of the surface where the flowers can no longer be observed after baking (see Fig. 5.5) However, in most HVAC&R applications, the environment temperature will typically be less than 50°C; thus, these observed changes may not pose significant problems.



Figure 5.4 Surface with contact angle of 108 degree after baked at 100°C for 10 min

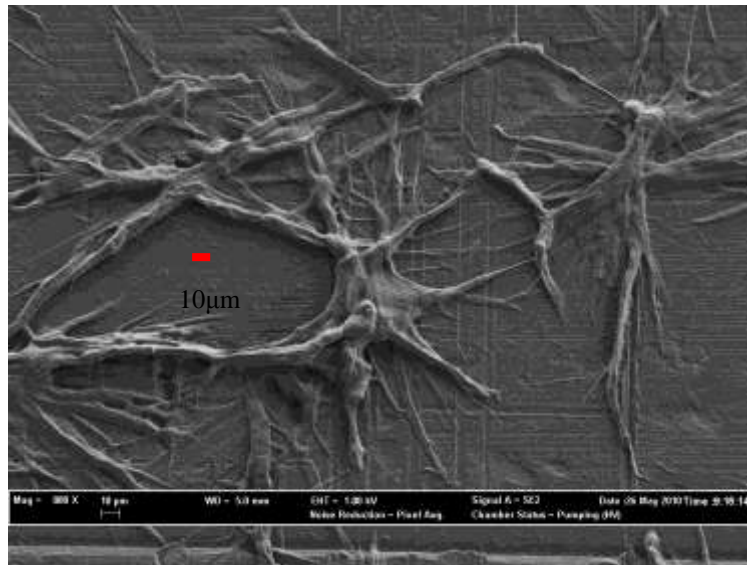


Figure 5.5 SEM image of surface after baked at 100°C for 10 min

5.2.3 Creating Chemical Stripes with Hydrophobic Micro-channels

Micro-channels on the surface can be used to provide a path for droplets to drain, thereby reducing the air-side core pressure drop as proposed in this research. Creating micro channels is a controlled way of changing surface wettability and thus can be tailored to the application. Likewise, hydrophobic stripes can be added to a hydrophilic surface in a controlled manner to change the surface wettability as desired.

Using the same photolithography practices, without wet etching, stripes of photoresist can be formed on the surface. Afterwards, the hydrophobic material can be deposited on the unprotected area by immersing the sample in the solution. After removing the photo resist, the surface will remain with potentially super hydrophobic stripes. A negative photo resist KMPR 1005 was used instead of the positive resist S1813 because S1813 is attacked by *n*-tetradecanoic acid. The resist KMPR was found survive in the 0.02 M *n*-tetradecanoic acid solution for at least two days. Sulfuric acid was also used before immersing to remove the native oxide. The sample was immersed in the 0.02 M solution for two days.

The recipe for making hydrophobic stripes on the copper surface is as follows:

1. Sample preparation:
 - Clean the copper plate with ultrasonic bath for 10 minutes
 - Clean the surface with Alconox for 15 minutes
 - Use acetone and IPA
2. Spin the photoresist KMPR 1005 in two steps:
 - (1) 500 rpm for 10 seconds
 - (2) 6000 rpm for 40 seconds
3. Bake the plate at 100°C for 5 minutes using a hotplate
4. Expose the sample for 20 seconds using the mask aligner.
5. Post exposure bake at 100°C for 2 minutes
6. Develop the surface in CD 26 (1:1 with water) for 40 s
7. Immerse the sample in sulfuric acid (acid: water = 2:500) for 20 seconds
8. Transfer the sample to the solution of *n*-teradecanoic acid (0.02 M) for electrodeposition
9. Clean the surface with water and ethanol
10. Lift off the photoresist using acetone and MICROPOSIT REMOVER 1165

5.3 Results and Conclusion

After lifting the photoresist, the surface was characterized using an optical microscope and a SEM. Stripes can be observed on most area of the surface (see Fig. 5.6 and Fig. 5.7). In the SEM images, the clusters which formed the stripes can be observed clearly; however, these structures look different than the flower-like clusters observed in Fig. 5.3. The different immersion time may have caused these differences in the copper carboxylate. Additionally, the edge of the photoresist may also affect the deposition.



Figure 5.6 Optical microscope image of the copper surface with stripes (black)

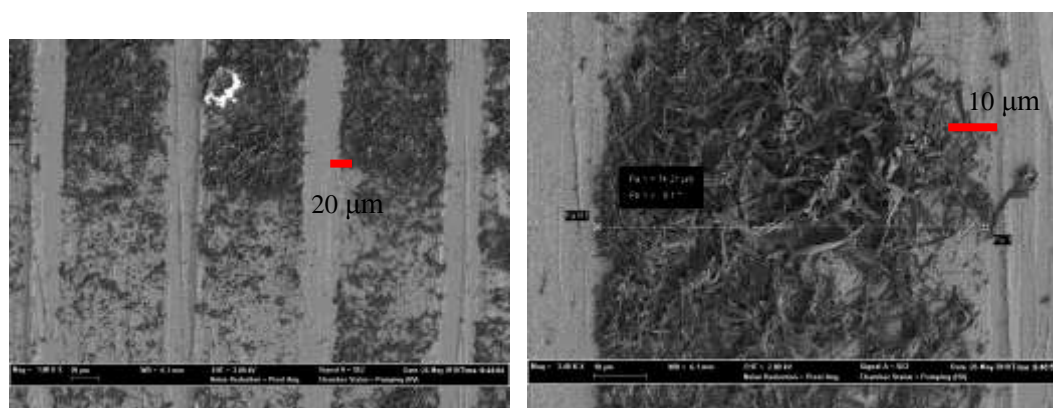


Figure 5.7 SEM images of copper surface with stripes.

The apparent contact angle was also measured for this surface and was found to be 106° which is smaller than the contact angle of the surface homogeneously covered

with the clusters. This is probably due to presence of the hydrophilic copper stripes on the surface. Because copper is naturally hydrophilic, if the edge of a droplet was placed on the copper stripe, the contact angle would be expected to be smaller (see Fig 5.8).



Figure 5.8 Surface with stripes: contact angle on the left is larger than right

Water behavior was also studied for this hydrophilic copper surface with hydrophobic stripes. A small droplet was placed on the stripes and observed under an optical microscope. The contact line of the droplet was observed to vary with the different surface wettabilities (see Fig. 5.9). The contact line of the surface is no longer a smooth circle—a wavy, or wrinkled line can clearly be observed. On the hydrophobic area, the droplet seems to slightly retract from the surface. On the hydrophilic area, the droplet was dragged by the surface tension. This unusual contact line behavior was discussed by other researchers as well. L. BORUVKA et al studied surface with alternating parallel strips of two different materials with different contact angle values [36].

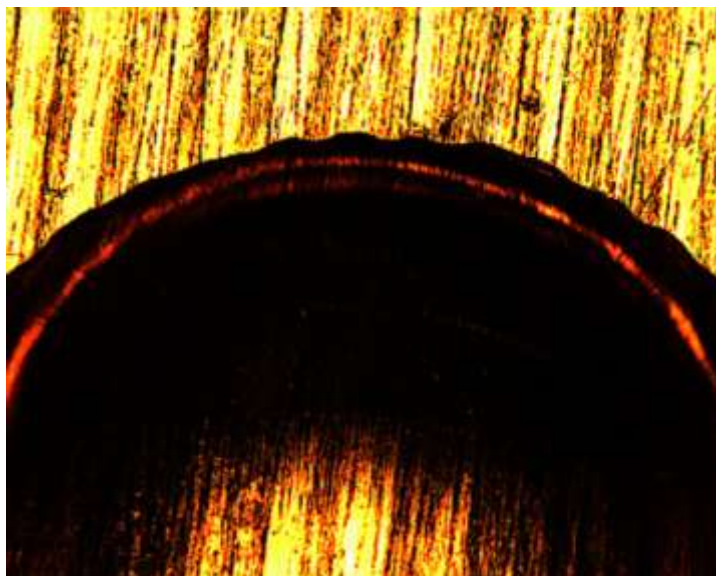


Figure 5.9 Top image of a small droplet on the surface with stripes.

Chapter 6 Conclusion and Recommendations

This research study was aimed at finding an efficient way of manufacturing surfaces with an anisotropic wettability (i.e. hydrophobic/hydrophilic). The overall goal was to understand the water droplet behavior on these modified surfaces in order to improve upon current fin surface designs. Experiments were conducted to develop a recipe for manufacturing these novel anisotropic surfaces, and the wettability parameters of these surfaces were studied. In addition, a general model to predict the critical air-flow velocity was developed. An initial model from the literature was also validated for these surfaces, and a new way of producing super-hydrophobic stripes on metallic surfaces was explored.

6.1 Summary of Results

6.1.1 Surface Manufacturing

- The aluminum plates were pre-roughened by immersion in a NaOH aqueous solution to increase the initial surface roughness.
- Different sizes parallel micro-grooves (15 μm , 50 μm , 100 μm) were transferred from the photomask to Al plates using standard photolithographic practices.
- Transene Aluminum Etchant Type A was used to etch the Al plates and create the micro-channels on the surface..
- Poly(dimethylsiloxane) vinyl terminated (PDMSVT) was spin-coated onto the Al surface as a hydrophobic coating.

6.1.2 Surface Parameter Measurements

- *Contact Angles:* Contact angles were measured using a RaméHart precision contact angle goniometer. For the baseline surface, the measured advancing

contact angle was 107.1° and the receding contact angle was 75.2° . The hysteresis of the baseline Al surface only reduced slightly from 31.9° to 29.3° after the application of the PDMS coating to the surface. By creating micro-channels on the surface, the contact angle hysteresis for Sample 1 (channel depth = $10\text{ }\mu\text{m}$) increased to 66.0° , 70.5° , and 76.1° for the $15\mu\text{m}$, $50\mu\text{m}$, and $100\mu\text{m}$ wide channels, respectively. **Thus, the addition of the micro-channels made the surface more hydrophilic. After the surface with channels was spin-coated with PDMS, the surface was found to be hydrophobic with a significantly reduced hysteresis of up to approximately 50 %.**

- *Critical Inclination Angles:* The critical inclination angle for sliding on these surfaces was measured using a tilt-table assembly with an extendable lever arm that permitted continuous inclination of the surface from horizontal. The baseline surface exhibited much higher critical inclination angles for sliding for a droplet of a given volume than the wet-etched anisotropic surfaces. With respect to sample 2, the reduction in the critical inclination angle was observed to be more pronounced for larger droplet volumes. **The difference in the measured critical inclination angles between sample 1 and sample 2 also suggested that sample 1 is more hydrophobic than sample 2. This observation implies that deeper channels have a more significant effect on the wettability of the surface than shallower channels.** These data were then compared to the predicted critical droplet volume as given by Dussan [27]. It was also observed that larger critical angles of inclination were manifested by sample 1 in the perpendicular configuration as compared to the parallel configuration.
- *Air-Flow Induced Droplet Movement:* These experiments were conducted in a open-circuit wind tunnel. The hydrophilic surface (sample 3) required larger air-flow rates for the onset of droplet motion than the baseline surface for droplet volumes between 5 and $25\text{ }\mu\text{L}$. **The surface with the micro-channels and PDMS coating was found to reduce the critical air-flow force as compared to the**

baseline surface.

- Similar to the injected droplet data, condensed droplet data also suggested that sample 1 was more effective at draining water than the baseline surface. On the baseline surface, the test results showed that the critical inclination angles were smaller for the condensed droplets than the injected droplets, whereas on sample 1, the injected droplets were observed to have smaller critical inclination angles than the condensed droplets.
- The water evaporation rate was also studied for the range of droplet volumes examined (i.e. 5 μL - 70 μL). The effect of evaporation was not found to be significant for the duration the tests were performed.

6.1.3 Water Droplet Modeling

- A new model that includes the air flow force has been developed and may be used for predicting the “critical” air flow velocity necessary for water droplet shedding.
- A “two-circle method” was adopted to predict the projected area of droplets on vertical surfaces. Using two circles to fit the periphery of droplets was found to more accurately predict the droplet projected area than using a single circle.
- Equations relating the droplet diameter to the droplet volume were developed for use in the model by measuring the diameter of droplets injected onto these surfaces using the precision contact angle goniometer. Functions were developed for both the baseline surface and sample 1.
- In order to find the drag coefficient for $1500 < \text{Re} < 2500$, the critical air-flow velocity for droplet movement was measured on a flat horizontal plate. At each recorded condition, force balance equality between the surface tension and air-flow

force was used to infer the drag coefficient of the droplet. Using this approach, the average drag coefficient C_d was found to be 0.45.

- Droplets on a vertical surface were observed to slide at an angle with respect to the vertical when the critical air flow velocity was reached. To find the sliding angle φ of a droplet with respect to the vertical, an image of the droplet's initial position was recorded. Images were then taken when the droplet started moving and compared with the initial image to find the sliding angle.

- A general model was developed using the equations below:

Air flow force: $F_d = -C_d \rho_a u^2 A_{pr}$

where $C_d = 0.446$ and projected area was calculated using two-circle methods.

Gravitational force: $F_{gx} = -\rho g V \sin \alpha$

Surface tension force: $F_{sx} = -A \psi \gamma \int_0^{2\pi} \zeta \cos \theta \cos (\theta - \varphi) d\theta$

where $A=1.285$, or for baseline surfaces:

$$\frac{F_s}{\gamma R} = k \cdot \psi \cdot (\cos \theta_R - \cos \theta_A)$$

where $\psi = \frac{w_1 + 2d + w_2}{w_1 + w_2}$ and $k=1.96$.

Forces balance: $F_s + F_d + F_g = 0$

Inputs of the model: Droplet volume V , advancing and receding contact angles, and ψ

Output of the model: Critical air-flow velocity u

This developed model was then tested for the baseline surface, sample 1, sample 2, and sample 3.

6.1.4 Manufacturing of hydrophobic stripes

- A method was developed for creating hydrophobic micro-scale stripes on a copper surface using standard photolithography. The hydrophobic material was deposited on the unprotected area by immersing the sample in a solution of

n-tetradecanoic acid. Electrochemistry using a 6V battery was shown to speed up the reaction time.

- Apparent contact angles measured on homogeneously modified copper surfaces were larger than 130°. Flower-like clusters were also observed on these surfaces.
- The apparent contact angle measured on a surface with the micro-scale stripes was found to be 106° which is smaller than the contact angle on the surface homogeneously covered with the clusters.
- The water droplet contact line on this surface was no longer a smooth circle but instead exhibited waviness due to the anisotropy of the surface.
- Thermal stability tests performed on the homogeneously modified surface at 100°C for 10 minutes showed a degradation of the flower-like structures and a reduction in the apparent contact angle.

6.2 Recommendations for Future Work

This research used PDMS as the hydrophobic chemical coating. The layer of PDMS applied to the surfaces in this work, however, was found to be relatively thick which may mitigate the influence of the underlying microstructure on the droplet. Thus, an alternative coating could be used such as an alkyl silane. Silanes are sometimes used on glass as a water repellent. The advantage is that the silane is deposited on the surface as a thin layer.

The general model developed in this research was found to successfully predict overall trends and changes in surface wettability. However, the current model was designed for one particular type of surface roughness (i.e. parallel micro-channels). Thus, perhaps a more general method for handling other types of micro-structural surface roughness could be developed. If necessary, the model's accuracy could also be increased by incorporating more experimental data.

Finally, this research explored several new methods of manufacturing hydrophobic surfaces including the use of both micro-channels and micro-stripes. However, further research is still needed to assess the long-term durability and robustness of these surfaces for use in HVAC&R applications.

References

- [1] Energy Information Administration, *International Energy Outlook 2007*, United States Department of Energy, Washington, D.C., web site: www.eia.doe.gov/oiaf/ieo/index.html, retrieved on 2007-06-06.
- [2] Energy Information Administration, *State Energy Data 2004: Consumption*, Washington, D.C., web site: www.eia.doe.gov/emeu/states/sep_sum/plain_html/rank_use.html, retrieved on 2007-09-29.
- [3] H. Tavana, A. Amirfazli, and A. W. Neumann, "Fabrication of Superhydrophobic Surfaces of *n*-Hexatriacontane", *Langmuir* 2006, 22, 5556-5559
- [4] Zhang, X.; Jin, M.; Liu, Z.; Tryk, D. A.; Nishimoto, S.; Murakami, T.; Fujishima, A. J. Phys. Chem. C 2007, 111, 14521–14529.
- [5] L. Rizzello, S. Shiv Shankar, D. Fragouli, A. Athanassiou, R. Cingolani, and P. P. Pompa, "Microscale Patterning of Hydrophobic/Hydrophilic Surfaces by Spatially Controlled Galvanic Displacement Reactions", *Langmuir* **2009**, 25(11), 6019–6023
- [6] Shibuichi, S., Yamamoto, T., Onda, T., Tsujii, K., 1998, Super water- and oil-repellent surfaces resulting from fractal structure, *J. Colloid Interface Sci.* **208**, pp.287-294.
- [7] Qian, B., Shen, Z., 2005, Fabrication of superhydrophobic surfaces by dislocation-selective chemical etching on aluminum, copper, and zinc substrates, Letters in *Langmuir*, pp. A-C.
- [11] Guo, Z.G., Zhou, F., Hao, J.C., Liu, W.M., 2005, *J. Am. Chem. Soc.* 127, 15670.
- [12] Bayiati, P., Tserepi, A., Gogolides, E., Misiakos, K., 2004, Selective plasma-induced deposition of fluorocarbon films on metal surfaces for actuation in microfluidics, *J. Vac. Sci. Technol.* **22**(4), pp. 1546-1551.
- [13] Ji, H., Côté A., Koshel, D., Terreault, B., Abel, G., Ducharme, P., Ross, G., Savoie, S., Gagné M., 2002, Hydrophobic fluorinated carbon coatings on silicate glaze and aluminum, *Thin Solid Films* **405**, pp. 104-108.
- [14] Somlo, B., Gupta, V., 2001, A hydrophobic self-assembled monolayer with improved adhesion to aluminum for deicing application, *Mech. of Materials* **33**, pp. 471-480.

- [15] Sommers, A.D. and Jacobi, A.M., 2006, Creating micro-scale surface topology to achieve anisotropic wettability on an aluminum surface, *J. Micromech. Microeng.* 16, pp.1571–1578
- [16] Korte, C.M. and Jacobi, A.M., 1997, “Condensate Retention and Shedding Effects of Air-Side Heat Exchanger Performance,” TR-132, ACRC, University of Illinois, Urbana.
- [17] Korte, C.M. and Jacobi, A.M., 2001, “Condensate Retention Effects on the Performance of Plain-Fin-and-Tube Heat Exchangers: Retention Data and Modeling,” *J. Heat Transfer*, Vol. 123, pp. 926-936.
- [18] Graham, C., 1969, “The Limiting Heat Transfer Mechanisms of Dropwise Condensation,” Ph.D. thesis, Massachusetts Institute of Technology, MA.
- [19] Merte, H. and Yamali, C., 1983, “Profile and Departure Size of Condensation Drops on Vertical Surfaces,” *Warme Und Stoffubertragung-Thermo and Fluid Dynamics*, Vol. 17, pp. 171-180.
- [20] Goodwin, R., Rice, D., and Middleman, S., 1988, “A Model for the Onset of Motion of a Sessile Liquid-Drop on a Rotating-Disk,” *J. Colloid and Interface Science*, Vol. 125, pp. 162-169.
- [21] Cassie, A.C., and Baxter, S., 1944, *Trans. Faraday Soc.* 40, p. 546.
- [22] Öner, D., McCarthy, T.J., 2000, Ultrahydrophobic surfaces: effects of topography length scales on wettability, *Langmuir* **16**, pp. 7777–7782.
- [23] Chen W, Fadeev A Y, Hsieh M C, Öner D, Youngblood J and McCarthy T J, 1999, Ultrahydrophobic and ultralyophobic surfaces: some comments and examples, *Langmuir* **15**, pp. 3395–3399.
- [24] Jopp J, Grüll H and Yerushalmi-Rozen R 2004 Wetting behavior of water droplets on hydrophobic microtextures of comparable size *Langmuir* **20**, pp. 10015–10019.
- [25] Fürstner R, Barthlott W, Neinhuis C and Walzel P 2005 Wetting and self-cleaning properties of artificial superhydrophobic surfaces *Langmuir* **21** 956–61
- [26] Dussan V E B, Chow R T-P, 1983, On the ability of drops or bubbles to stick to non-horizontal surfaces of solids *J. Fluid Mech.* **137**, p. 1–29.
- [27] Dussan V E B, 1985, On the ability of drops or bubbles to stick to non-horizontal surfaces of solids: Part 2. Small drops of bubbles having contact angles of arbitrary size, *J. Fluid Mech.* **151**, pp. 1–20.

- [28] A.I. El Sherbini, Modeling Condensate Drops Retained on the Air-Side of Heat Exchangers, Ph.D. thesis, Univ. of Illinois at Urbana–Champaign, Urbana, 2003
- [29] Wolfram, E. and Faust, R., 1978, “Liquid Drops on a Tilted Plate, Contact Angle Hysteresis and the Young Contact Angle,” In *Wetting, Spreading, and Adhesion*, J.F. Padday, Ed. New York: Academic Press.
- [30] Extrand, C.W. and Gent, A.N., 1990, “Retention of Liquid Drops by Solid Surfaces,” *J. Colloid and Interface Science*, Vol. 138, pp. 431-442.
- [31] A.I. El Sherbini and A.M. Jacobi, Liquid drops on vertical and inclined surfaces I. An experimental study of drop geometry, *Journal of Colloid and Interface Science* 273 (2004) 556–565
- [32] A.I. El Sherbini, A.M. Jacobi, “Liquid drops on vertical and inclined surfaces: II. A method for approximating drop shapes,” *J. Colloid Interface Sci.* **273**, (2004) 566-575.
- [33] Al-Hayes, R. A. M., and Winterton, R. H. S., 1981, “Bubble Diameter on Detachment in Flowing Liquids,” *Int. J. Heat Mass Transf.*, 24, pp. 223-230
- [34] Shutao Wang, Lin Feng, and Lei Jiang, ”One-Step Solution-Immersion Process for the Fabrication of Stable Bionic Superhydrophobic Surfaces,” *Adv. Mater.* 2006, 18, pp. 767-770
- [35] Preeti S. Yadav, Prashant Bahadur, Rafael Tadmor, Kumud Chaurasia and Aisha Leh, ”Drop Retention Force as a Function of Drop Size”, *Langmur* 2008,24, 317-3184
- [36] L. BORUVKA AND A. W. NEUMANN, “An Analytical Solution of the Laplace Equation for the Shape of Liquid Surfaces Near a Stripwise Heterogeneous Wall”, *Journal of Colloid and Interface Science*, Vol. 65, No. 2, June 15, 1978

Appendix A: Model for Horizontal Surfaces

In this appendix, a program generating a model for horizontal baseline surface is presented. This model can be used to calculate the drag coefficient C_d and Reynolds number. The program is listed below: (inputs of this program is highlighted)

{* Program to calculate the drag coefficient for water droplets on a Horizontal Al surface***}**

$$Bo = \rho \cdot g \cdot \sin(\alpha_{\text{rad}}) \cdot D^2 / \Gamma \cdot 10^{-3}$$

$$\text{Beta} = 1 + 0.096 \cdot Bo$$

$$L = \text{Beta}^{0.5} \cdot D / 2$$

$$\theta_{\text{Arad}} = \alpha \cdot \pi / 180$$

$$\theta_{\text{min_rad}} = \text{rec} \cdot \pi / 180 \quad \text{\textit{--Contact Angle Variation Around the Base of the Droplet--}}$$

{---Theta Function---}

$$A = -(2 \cdot \theta_{\text{min_rad}} - 2 \cdot \theta_{\text{Arad}}) / \pi^3$$

$$B = -(3 \cdot \theta_{\text{Arad}} - 3 \cdot \theta_{\text{min_rad}}) / \pi^2$$

$$\zeta = L / (\cos(\text{Fi})^2 + \text{Beta}^2 \cdot \sin(\text{Fi})^2)^{0.5}$$

$$\theta_1 = A \cdot \text{Fi}^3 + B \cdot \text{Fi}^2 + \theta_{\text{Arad}}$$

$$\theta_2 = A \cdot (\pi - \text{Fi})^3 + B \cdot (\pi - \text{Fi})^2 + \theta_{\text{Arad}}$$

{---Forces---}

$$I_f = (\sin(\alpha) \cdot (1 - \cos(\text{rec}))) / (\sin(\text{rec}) \cdot (1 - \cos(\alpha)))$$

$$I_1 = D \cdot I_f / (1 + I_f)$$

$$I_2 = D / (1 + I_f)$$

$$F_d = 0.5 \cdot C_d \cdot \rho_{\text{air}} \cdot (V_{\text{el}}^2) \cdot A_{\text{pr}} \cdot 10^{-3} \quad \text{\textit{air-flow force}}$$

$$\theta_M = (\theta_{\text{min_rad}} + \theta_{\text{Arad}}) / 2$$

$$A_{\text{pr}} = ((D^2) \cdot \theta_M / 4) - ((D^2) / 4) \cdot \cos(\theta_M) \cdot \sin(\theta_M) \cdot (1 / ((\sin(\theta_M))^2))$$

{projected area on a horizontal baseline surface}

$$\rho_{\text{air}} = \text{Density}(\text{Air}, T=20, P=101)$$

$$\mu_{\text{air}} = \text{Viscosity}(\text{Air}, T=20)$$

$$\text{Re}_D = (\rho_{\text{air}} \cdot V_{\text{el}} \cdot D) / (\mu_{\text{air}}) \quad \text{\textit{Reynolds number for these tests}}$$

$$\text{Re}_{D_{\text{typical}}} = (\rho_{\text{air}} \cdot 1.5 \cdot D) / (\mu_{\text{air}}) \quad \text{\textit{Reynolds number typical to application}}$$

$$V_{\text{el}} = 7.51 \quad \text{\textit{air-flow velocity, m/s}}$$

```

dFs_1=zeta*cos(theta_1)*cos(Fi)
dFs_2=zeta*cos(theta_2)*cos(pi+Fi)
int_1=integral(dFs_1,Fi,0,pi/2)
int_2=integral(dFs_2,Fi,0,pi/2)
Fs=2*1.285*Gamma*(int_1+int_2)           {Surface Tension Force}
F_diff=Fs+F_d
F_diff=0
{---MAIN---}
{--PROGRAM INPUTS--}
adv=107.129                               {Rec. Contact Angle, deg,base_line}
rec=75.205                                {Adv. Contact Angle, deg,base_line}
alpha=0                                   {Surface Inclination Angle, deg}
Vol1=60*1e-6                             {Droplet Volume, L}
contact_angle= 84.9                      {Apparent contact angle}
theta_contact=contact_angle*pi/180
Vol=Vol1*convert(L,m^3)                   {Droplet Volume, m^3}
Vol= (pi*(D^3)/24)*((2-3*cos(theta_contact)+(cos(theta_contact))^3)/((sin(theta_contact))^3))
{Droplet diameter, m}
alpha_rad=alpha*pi/180                   {Surface Inclination Angle, rad}
rho=1000
Gamma=72.8                               {Surface Tension, mN/m}
g=9.81                                   {Density, kg/m^3}

```

Appendix B: Model for Vertical Surfaces

The program listed in this appendix is the general model presented in chapter 4 to predict the critical air-flow velocity for a given droplet volume on a vertical surface.

Model description:

$$\text{Air flow force: } F_d = -C_d \rho_a u^2 A_{pr}$$

where $C_d = 0.45$ and projected area was calculated using two-circle methods.

$$\text{Gravitational force: } F_{gx} = -\rho g V \sin \alpha$$

$$\text{Surface tension force: } F_{sx} = -A \gamma \int_0^\pi \zeta \cos \theta \cos (\theta - \varphi) d\theta$$

where $A=1.285$, and surfaces tension force on baseline surface can be calculated using the equation below:

$$\frac{F_s}{\gamma R} = k \cdot \psi \cdot (\cos \theta_R - \cos \theta_A)$$

where $\psi = \frac{w_1 + 2d + w_2}{w_1 + w_2}$ and $k=1.96$.

$$\text{Forces balance: } F_s + F_d + F_g = 0$$

Inputs of the model: Droplet volume V, Advancing and receding contact angle and ψ

Output of the model: Critical air-flow velocity u

Program:

```

{*** Program to calculate the critical droplet size for sliding for water droplets on an engineered
AI surface***}
{--INPUTS to the Lookup Table are:}
{alpha (degrees): surface inclination angle,}
{theta_A (degrees): advancing contact angle,}
{theta_rec(mm): receding contact angle,}
{--For other liquids, change density, rho (kg/m3) and surface tension, Gamma (mN/m)--}
{--Important Units: mass per unit area (g/m2); Diameters (mm), and Volume (mm3)--}
SUBPROGRAM Fbalance(alpha_rad, theta_Arad, V: theta_rec, F_diff)
$COMMON rho, g, Gamma
{--Forces acting on a drop--}
Bo=rho*g*sin(alpha_rad)*Dmm^2/Gamma*1e-3
Beta=1+0.096*Bo
Beta=L/w
L=Beta^.5*D/2
theta_rec=AvgLookup('Data1','theta_rec',1,1)
theta_min_rad=theta_rec*pi/180

```


{---Theta Function---}

$$A = -(2 * \theta_{\min_rad} - 2 * \theta_{Arad}) / \pi^3$$

$$B = -(3 * \theta_{Arad} - 3 * \theta_{\min_rad}) / \pi^2$$

$$\theta_1 = A * (F_i)^3 + B * (F_i)^2 + \theta_{Arad}$$

$$\theta_2 = A * (\pi - F_i)^3 + B * (\pi - F_i)^2 + \theta_{Arad}$$

$$\zeta = L / (\cos(F_i)^2 + \beta^2 \sin(F_i)^2)^{0.5}$$

{---Forces---}

$$F_g = -\rho * g * \sin(\alpha_{rad}) * Vol_m * 1e3 * \cos(\text{angle}) \quad \{\text{Gravitational Force in microNewton (10e-6 N)}\}$$

$$Vol_L = 21 \quad \{\text{Droplet Volume, uL}\}$$

$$D_{mm} = 1.6553 * Vol_L^{0.2906}$$

$$D_{mm} = 0.9804 * Vol_L^{0.4967}$$

$$D = D_{mm} / 1000 \quad \{\text{Droplet diameter, m}\}$$

$$\theta_M = (\theta_{\min_rad} + \theta_{Arad}) / 2$$

$$\text{angle_deg} = (0.0035 * Vol_L^5 - 0.195 * Vol_L^4 + 4.1084 * Vol_L^3 - 40.711 * Vol_L^2 + 186.95 * Vol_L - 292.94) \quad \{\text{Angle Function}\}$$

$$\text{angle} = \text{angle_deg} * \pi / 180$$

$$F_d = -0.5 * C_d * \rho_{air} * (V^2) * A_{pr} * 1e3 * \sin(\text{angle}) \quad \{\text{Air Flow Force}\}$$

$$I_f = (\sin(\theta_{Arad}) * (1 - \cos(\theta_{\min_rad})) / (\sin(\theta_{\min_rad}) * (1 - \cos(\theta_{Arad})))$$

$$I_1 = D * I_f / (1 + I_f)$$

$$I_2 = D / (1 + I_f)$$

$$A_{pr} = \pi * ((I_1^2) / ((\sin(\pi - \theta_{Arad}))^2)) * (\theta_{Arad} / (2 * \pi)) + 0.5 * (I_1^2) / (\tan(\pi - \theta_{Arad})) + \pi * ((I_2^2) / ((\sin(\theta_{\min_rad}))^2)) * (\theta_{\min_rad} / (2 * \pi)) - 0.5 * (I_2^2) / \tan(\theta_{\min_rad})$$

$$\rho_{air} = \text{Density}(\text{Air}, T=23, P=101)$$

$$\mu_{air} = \text{Viscosity}(\text{Air}, T=23)$$

$$\mu_{water} = \text{Viscosity}(\text{Water}, T=23, P=101)$$

$$\nu_{air} = \mu_{air} / \rho_{air}$$

$$Re_D = (\rho_{air} * V * (D_{mm} / 1000)) / (\mu_{air}) \quad \{\text{Reynolds number for these tests}\}$$

$$Re_{D_typical} = (\rho_{air} * 1.5 * (D_{mm} / 1000)) / (\mu_{air}) \quad \{\text{Reynolds number typical to application}\}$$

$$C_d = 0.4461$$

$$dF_{s_1} = \zeta * \cos(\theta_1) * \cos(F_i - \text{angle})$$

$$dF_{s_2} = \zeta * \cos(\theta_2) * \cos(\pi + F_i - \text{angle})$$

$$\text{int}_1 = \text{integral}(dF_{s_1}, F_i, 0, \pi)$$

$$\text{int}_2 = \text{integral}(dF_{s_2}, F_i, 0, \pi)$$

$$F_s = -1.285 * \text{factor} * \Gamma * (\text{int}_1 + \text{int}_2)$$

$$\text{factor} = 1.24$$

$$F_{s_check} = -(D/2) * k * \Gamma * (\cos(\theta_{Arad}) - \cos(\theta_{\min_rad}))$$

{Gravitational Force in microNewton (10e-6 N)}

$$k = 1.96$$

$$F_{diff} = F_s + F_g + F_d$$

```

F_diff=Fs_check+Fg+F_d
END
PROCEDURE MAXDIAM(alpha_rad, theta_Arad: V_max, theta_rec)
$COMMON rho, g, Gamma
{---Maximum diameter of a drop from a force balance---}
{Procedure may be modified to use other optimization methods}
V=0.1 {Air Velocity, m/s}
delta_V=0.5
10: V:=V+delta_V
call Fbalance(alpha_rad, theta_Arad, V: theta_rec, F_diff)
IF (F_diff>0) THEN GOTO 10
IF (delta_V>0.01) THEN
    V:=V-delta_V
    delta_V:=delta_V/2
    GOTO 10
ENDIF
V_max=V
END
{---MAIN---}
alpha=AvgLookup('Data1','alpha',1,1)
theta_A=AvgLookup('Data1','theta_A',1,1)
theta_Arad=theta_A*pi/180
alpha_rad=alpha*pi/180
rho=1000 {kg/m^3}
Gamma=72.8 {mN/m}
g=9.81 {m/s^2}
call MAXDIAM(alpha_rad, theta_Arad: V_max, theta_rec)

```